

This work was written as part of one of the author's official duties as an Employee of the United States Government and is therefore a work of the United States Government. In accordance with 17 U.S.C. 105, no copyright protection is available for such works under U.S. Law.

Public Domain Mark 1.0

<https://creativecommons.org/publicdomain/mark/1.0/>

Access to this work was provided by the University of Maryland, Baltimore County (UMBC) ScholarWorks@UMBC digital repository on the Maryland Shared Open Access (MD-SOAR) platform.

**Please provide feedback**

Please support the ScholarWorks@UMBC repository by emailing [scholarworks-group@umbc.edu](mailto:scholarworks-group@umbc.edu) and telling us what having access to this work means to you and why it's important to you. Thank you.



# Simultaneous retrieval of aerosol and ocean properties from PACE HARP2 with uncertainty assessment using cascading neural network radiative transfer models

Meng Gao<sup>1,2</sup>, Bryan A. Franz<sup>1</sup>, Peng-Wang Zhai<sup>3</sup>, Kirk Knobelspiesse<sup>1</sup>, Andrew M. Sayer<sup>1,3</sup>, Xiaoguang Xu<sup>3</sup>, J. Vanderlei Martins<sup>3</sup>, Brian Cairns<sup>4</sup>, Patricia Castellanos<sup>6</sup>, Guangliang Fu<sup>7</sup>, Neranga Hannadige<sup>3</sup>, Otto Hasekamp<sup>7</sup>, Yongxiang Hu<sup>5</sup>, Amir Ibrahim<sup>1</sup>, Frederick Patt<sup>1,8</sup>, Anin Puthukkudy<sup>3</sup>, and P. Jeremy Werdell<sup>1</sup>

<sup>1</sup>Ocean Ecology Laboratory, NASA Goddard Space Flight Center, Greenbelt, MD 20771, USA

<sup>2</sup>Science Systems and Applications, Inc., Greenbelt, MD, USA

<sup>3</sup>University of Maryland, Baltimore County, Baltimore, MD 21250, USA

<sup>4</sup>NASA Goddard Institute for Space Studies, New York, NY 10025, USA

<sup>5</sup>NASA Langley Research Center, MS 475, Hampton, VA 23681-2199, USA

<sup>6</sup>Global Modeling and Assimilation Office, NASA Goddard Space Flight Center, Greenbelt, MD 20771, USA

<sup>7</sup>Netherlands Institute for Space Research (SRON, NWO-I), Leiden, the Netherlands

<sup>8</sup>Science Applications International Corp., Greenbelt, MD, USA

**Correspondence:** Meng Gao (meng.gao@nasa.gov)

Received: 12 August 2023 – Discussion started: 29 August 2023

Revised: 7 October 2023 – Accepted: 22 October 2023 – Published: 7 December 2023

**Abstract.** The University of Maryland, Baltimore County (UMBC) Hyper-Angular Rainbow Polarimeter (HARP2) will be on board NASA's Plankton, Aerosol, Cloud, ocean Ecosystem (PACE) mission, scheduled for launch in January 2024. In this study we systematically evaluate the retrievability and uncertainty of aerosol and ocean parameters from HARP2 multi-angle polarimeter (MAP) measurements. To reduce the computational demand of MAP-based retrievals and maximize data processing throughput, we developed improved neural network (NN) forward models for spaceborne HARP2 measurements over a coupled atmosphere and ocean system within the FastMAPOL retrieval algorithm. To this end, a cascading retrieval scheme is implemented in FastMAPOL, which leverages a series of NN models of varying size, speed, and accuracy to optimize performance. Two sets of NN models are used for reflectance and polarization, respectively. A full day of global synthetic HARP2 data was generated and used to test various retrieval parameters including aerosol microphysical and optical properties, aerosol layer height, ocean surface wind speed, and ocean chlorophyll *a* concentration. To assess retrieval quality, pixel-wise retrieval uncertainties were derived from error propagation and evaluated against the difference between the retrieval pa-

rameters and truth based on a Monte Carlo method. We found that the fine-mode aerosol properties can be retrieved well from the HARP2 data, though the coarse-mode aerosol properties are more uncertain. Larger uncertainties are associated with a reduced number of available viewing angles, which typically occur near the scan edge of the HARP2 instrument. Results of the performance assessment demonstrate that the algorithm is a viable approach for operational application to HARP2 data after the PACE launch.

## 1 Introduction

Satellite remote sensing has greatly enhanced our understanding of the Earth's environment, including the characterization of atmospheric aerosols and surface properties (Kaufman et al., 2002; Kokhanovsky et al., 2015; Kahn, 2015; Pörtner et al., 2023). Multi-angle polarimetric (MAP) remote sensing, pioneered by the Polarization and Directionality of the Earth's Reflectances (POLDER) instrument on Advanced Earth Observing Satellites (ADEOS-I; 1996–1997 and ADEOS-II; 2002–2003) and the Polarization and

Anisotropy of Reflectances for Atmospheric Sciences coupled with Observations from a Lidar (PARASOL; 2004–2013) mission (Tanré et al., 2011), has emerged as a promising approach for retrieving geophysical properties from Earth observations (Mishchenko and Travis, 1997; Hasekamp and Landgraf, 2007; Knobelspiesse et al., 2012; Lacagnina et al., 2017; Dubovik et al., 2019; Hasekamp et al., 2019b; Chen et al., 2022).

This trend is set to continue with the forthcoming launch of the National Aeronautics and Space Administration (NASA) Plankton, Aerosol, Cloud, ocean Ecosystem (PACE) mission in January 2024, featuring a hyperspectral scanning radiometer named the Ocean Color Instrument (OCI) (Meister et al., 2022) and two MAPs with high polarimetric accuracy: the University of Maryland, Baltimore County (UMBC) Hyper-Angular Rainbow Polarimeter (HARP2) (Martins et al., 2018; McBride et al., 2023) and the Netherlands Institute for Space Research (SRON) Spectro-Polarimeter for Planetary EXploration one (SPEXone) (Hasekamp et al., 2019a; Smit et al., 2019). The deployment of these instruments presents an unprecedented opportunity to enhance our understanding and representation of atmospheric and surface conditions (Remer et al., 2019a, b; Frouin et al., 2019) and bridge future MAP observations, such as the European Space Agency (ESA) Multi-viewing Multi-channel Multi-polarisation Imager (3MI) on board the MetOp-SG satellites (Fougnie et al., 2018) and NASA's Multi-Angle Imager for Aerosols (MAIA) instrument (Diner et al., 2018).

Advanced simultaneous aerosol and surface property retrieval algorithms have been developed for MAP instruments (Chowdhary et al., 2005; Waquet et al., 2009; Hasekamp et al., 2011, 2019b; Dubovik et al., 2011, 2014; Wang et al., 2014; Wu et al., 2015; Xu et al., 2016, 2021; Fu and Hasekamp, 2018; Li et al., 2018, 2019; Stamnes et al., 2018, 2023; Gao et al., 2018, 2021a, 2023; Chen et al., 2020; Fu et al., 2020; Puthukkudy et al., 2020). Most of these retrieval algorithms developed for MAP observations are based on iterative optimization approaches that utilize vector radiative transfer (RT) forward models, capable of deriving atmospheric and surface properties simultaneously. Constrained by the speed of forward model calculations, MAP retrieval algorithms are often computationally expensive, which limits their applicability for large-scale operational data production and makes it difficult to conduct comprehensive uncertainty analyses. To address the data processing challenge related to the MAP instruments, Di Noia et al. (2015) developed a neural-network-based (NN-based) retrieval algorithm that derives aerosol properties directly from groundSPEX (a ground-based version of the SPEX instrument) and RSP (Research Scanning Polarimeter; Cairns et al., 1999) measurements. These directly inverted properties were then used as initial values in a subsequent iterative optimization.

To further improve the processing efficiency and flexibility, NN-based forward models are sometimes introduced to replace the radiative transfer calculation partially or fully in

the retrieval algorithms. For example, Fan et al. (2019) represented the polarimetric reflectance for an open-ocean system using an NN and applied it to SPEXone data processing by coupling it with a linearized radiative transfer atmosphere model (Hasekamp and Landgraf, 2005). The PACE HARP2 data pose a further challenge due to the large data volume, with a swath more than an order of magnitude wider than SPEXone's. Gao et al. (2021a) demonstrated that an NN-based forward model can be trained to represent the vector radiative transfer calculation on a fully coupled atmosphere and ocean system. To process HARP2 data efficiently, the FastMAPOL algorithm was developed, powered by such an NN-based radiative transfer forward model, and validated using AirHARP field campaign measurements (Gao et al., 2021a, b) and HARP2 synthetic data (Gao et al., 2021b, 2022). To facilitate data synergy from multiple PACE instruments, Stamnes et al. (2023) utilized NN-based forward models that combine spectral bands from both HARP2 and SPEXone in MAP retrievals. These recent developments build upon the successful application of NNs in non-polarimetric remote sensing (Diego and Loyola, 2004; Schroeder et al., 2007; Fan et al., 2017; Chen et al., 2018; Nanda et al., 2019; Shi et al., 2020; Ukkonen, 2022; Stegmann et al., 2022; Ibrahim et al., 2022) and achieve the high radiometric and polarimetric accuracy of modern MAPs by using a larger number of hidden layers (e.g., three layers) and nodes (usually 200–1000).

Building from these studies, this work presents a refinement of the FastMAPOL retrieval algorithm suitable for global-scale PACE HARP2 data processing. The NN forward model is further optimized based on a realistic training data set, including expected orbital satellite geometries and employing highly accurate vector radiative transfer simulations. This allows us to test the processing performance on global spaceborne data and illustrate the expected aerosol and ocean color retrieval performance of HARP2. We introduce a novel measurement-uncertainty-aware NN training via modification of its cost function, resulting in an NN accuracy more consistent with the retrieval's cost function. Additionally, we explore the trade-off between NN speed and accuracy, training different sizes of NNs based on the new cost function, and further propose a cascading retrieval scheme that leverages a series of NN models of varying size, speed, and accuracy. Initial retrievals are conducted using faster and smaller but less accurate NN models, with subsequent retrievals performed using larger and slower but more accurate NN models.

To analyze the retrieval performance and uncertainties of these products, global over-ocean HARP2 radiative transfer simulations were generated using the most accurate NN forward model. This effort is a part of the day-in-the-life (DITL) prelaunch data processing test organized by the PACE Science Data Segment (SDS). Through the global-scale data analysis based on the cascading NN scheme in FastMAPOL, we examine the retrieval uncertainties for aerosol microphysical and optical properties in both fine and coarse modes, as

well as ocean surface wind speed and ocean chlorophyll *a*, with respect to the location, geometries, and distribution of geophysical properties. We have also included aerosol layer height (ALH) in the HARP2 retrieval products, as encouraged by the sensitivity studies conducted on RSP (Wu et al., 2016) and the HARP instrument (Xu et al., 2021). The quantification of aerosol uncertainty can greatly enhance its applicability in radiative forcing, air quality, and climate studies. Consequently, this study offers a holistic discussion on the retrieval algorithm and the resultant data products with their associated uncertainties for HARP2 in anticipation of the upcoming PACE mission.

This study presents the advancements made to the HARP2 aerosol and ocean retrieval algorithm for operational data processing, including various improvements in the radiative transfer model with more realistic representation of spaceborne measurements, effective NN training methodology, flexible NN architectures, and a cascading retrieval scheme with comprehensive uncertainty assessment. The paper is organized in four sections, including a description of the retrieval algorithm and NN forward model (Sect. 2), retrieval and uncertainty analysis of the global-scale simulations (Sect. 3), and conclusion with discussions (Sect. 4).

## 2 Improved FastMAPOL retrieval algorithm

This section provides an overview of the enhancements made to the FastMAPOL retrieval algorithm, with various improvements in the radiative transfer model, NN training methodologies, and retrieval schemes with cascading NN models.

### 2.1 Simultaneous aerosol and ocean retrieval algorithm

HARP2 measures Stokes parameters  $L_t$ ,  $Q_t$ , and  $U_t$  (where the subscript *t* represents total measurement) at 60 viewing angles at the 660 nm band and at 10 viewing angles at the 440, 550, and 870 nm bands (Puthukkudy et al., 2020; McBride et al., 2023). The total spectral measured reflectance ( $\rho_t(\lambda)$ ) and degree of linear polarization (DoLP or  $P_t(\lambda)$ ) are used in the retrieval inversion, which are defined as

$$\rho_t = \frac{\pi r^2 L_t}{\mu_0 F_0}, \quad (1)$$

$$P_t = \frac{\sqrt{Q_t^2 + U_t^2}}{L_t}, \quad (2)$$

where  $F_0$  is the extraterrestrial solar irradiance,  $\mu_0$  is the cosine of the solar zenith angle, and  $r$  is the Sun–Earth distance correction factor in astronomical units. Note that the circular polarization (Stokes parameter  $V_t$ ) is not measured by HARP instruments and is often, but not always, negligible for atmospheric studies (Kawata, 1978; Gassó and Knobelspiesse, 2022).

To derive aerosol and ocean information, the retrieval algorithm minimizes the cost function  $\chi^2$ , which quantifies the difference between the measurement and the forward model simulation (Rodgers, 2000):

$$\chi^2(\mathbf{x}) = \frac{1}{N} \sum_i \left( \frac{[\rho_t(i) - \rho_t^f(\mathbf{x}; i)]^2}{\sigma_\rho^2(i)} + \frac{[P_t(i) - P_t^f(\mathbf{x}; i)]^2}{\sigma_P^2(i)} \right), \quad (3)$$

where  $\rho_t$  and  $P_t$  are measurements, and  $\rho_t^f$  and  $P_t^f$  are the corresponding quantities computed from the forward model. The state vector  $\mathbf{x}$  contains all retrieval parameters. The subscript *i* stands for the index of the measurements at different viewing angles and wavelengths, and *N* is the total number of measurements used in the retrieval. The total uncertainties of the reflectance and DoLP used in the algorithm are denoted as  $\sigma_\rho$  and  $\sigma_P$ ; both have contributions from measurement uncertainties  $\sigma_m$  and forward model uncertainties  $\sigma_f$ . In this work, the estimated expected measurement uncertainties for HARP2 of 3 % on reflectance and 0.005 on DoLP are used (McBride et al., 2023). Note that the above assumes independence of spectral or angular correlation between uncertainties; for a more complete treatment, Eq. (3) should be represented in a matrix form using the error covariance matrix (Rodgers, 2000; Gao et al., 2023). Statistical methods such as autocorrelation analysis have been used to estimate angular correlation strength from AirHARP field measurements and may be applied to future HARP2 data (Gao et al., 2023), but at present the correlation strength is not well known, so the above form (equivalent to a diagonal covariance matrix) is used. The retrieval is an iterative procedure to minimize using the subspace trust-region interior reflective optimization approach (Branch et al., 1999) by varying the state parameters  $\mathbf{x}$ . In this work, the forward models are based on the NN discussed in the next sections, and the Jacobian matrices, used to determine the direction to update the state parameter, are computed based on automatic differentiation (Baydin et al., 2018) as formulated for the NN forward model (Gao et al., 2021b) and implemented within the deep learning framework (Osawa et al., 2019).

### 2.2 Coupled atmosphere and ocean radiative transfer model

The training data for the NN forward model are generated with a PACE-tailored vector radiative transfer model using the successive orders of scattering method (Zhai et al., 2022), with much better numerical accuracy than that of the HARP instruments (Gao et al., 2021a). An improved pseudo spherical shell (IPSS) correction is considered to improve the fidelity for larger solar and viewing zenith angles (Zhai and Hu, 2022). Reflectance and DoLP are simulated at the PACE satellite altitude (676 km above the Earth's surface); viewing and solar geometries are defined at the surface as shown in Fig. 1 based on the formulas derived in Zhai and Hu (2022).

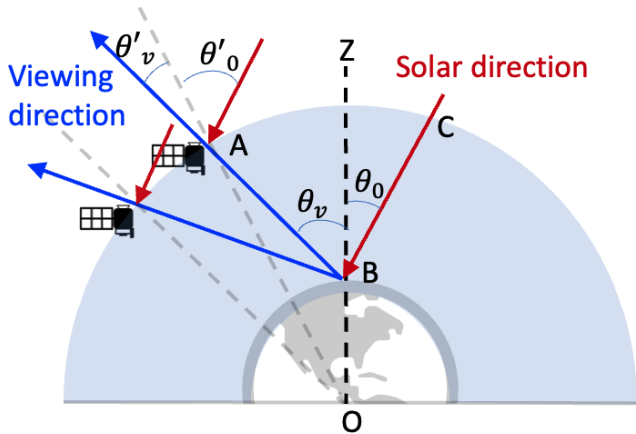


**Figure 1.** Spherical shell frame of the Earth system. The radiative transfer simulations are conducted according to the geometry defined at the satellite with the solar and viewing zenith angles  $\theta'_0$  and  $\theta'_v$ , which are converted to the geometry at the Earth's surface, with the solar and viewing zenith angles defined as  $\theta_0$  and  $\theta_v$ . The solar and viewing azimuthal angles also depend on the reference frame but are not shown in the figure.

The forward radiative transfer simulations are conducted assuming a coupled atmosphere and ocean system. The atmospheric molecule distributions follow the US standard atmospheric constituent profile (Anderson et al., 1986). Absorption by oxygen, water vapor, methane, carbon dioxide, ozone, and nitrogen dioxide is considered through line-by-line calculations and integrated based on the double-k method (Duan et al., 2005; Zhai et al., 2022). The ozone density and surface pressure are assumed in the range as defined in Table 1. Near the Earth's surface, an aerosol layer is considered with a vertical number density distribution assumed as a Gaussian function (Wu et al., 2015):

$$N(z) = \frac{N_t}{\sigma\sqrt{2\pi}} \exp\left(-\frac{(z - z_c)^2}{2\sigma^2}\right), \quad (4)$$

where  $N_t$  is the total aerosol column number density.  $z_c$  is defined as the aerosol layer height (ALH) in the range of 0.1 to 6 km above surface.  $\sigma$  is the standard deviation of the Gaussian distribution which is fixed at 2 km. The aerosol size is represented by the volume density of a combination of five lognormally distributed “submodes” similar to previous studies using the MAPOL (Gao et al., 2018) and FastMAPOL algorithms (Gao et al., 2021a). The mean radius  $r_i$  and standard deviation  $\sigma_i$  are fixed with values of 0.1, 0.1732, 0.3, 1.0, and 2.9  $\mu\text{m}$  and 0.35, 0.35, 0.35, 0.5, and 0.5, respectively, following the work by Dubovik et al. (2011), Xu et al. (2016), and Fu et al. (2020). The first three submodes are used to represent the fine-mode aerosol, while the last two submodes are the coarse mode. Fine and coarse modes are assumed to have an independent complex refractive index with no spectral variation within the HARP spectral range. Therefore, the aerosol model includes 10 parameters: five volume

**Table 1.** Parameters used to represent the coupled atmosphere and ocean system in the radiative transfer simulation and NN training.  $\theta_0$  and  $\theta_v$  are the solar and viewing zenith angles.  $\phi_v$  is the relative azimuth angle.  $V_i$  denotes the five volume densities. An aerosol optical depth (AOD) range from 0.01 to 0.5 is considered and used to constrain  $V_i$ .  $m_r$  and  $m_i$  are the real and imaginary parts of the refractive index. Additional parameters include ozone column density ( $n_{\text{O}_3}$ ), aerosol layer height ( $z_c$ ), surface pressure ( $P_s$ ), ocean surface wind speed ( $w_s$ ), and chlorophyll  $a$  concentration (Chl  $a$ ). The minimum (min) and maximum (max) values determine the parameter ranges used to generate NN training data, which are also the constraints in the retrieval algorithm.

Parameters	Unit	Min	Max
$\theta_0$	$^\circ$	0	85
$\theta_v$	$^\circ$	0	85
$\phi_v$	$^\circ$	0	180
$n_{\text{O}_3}$	Dobson	150	450
$m_{r,f}$	(None)	1.3	1.7
$m_{r,c}$	(None)	1.3	1.7
$m_{i,f}$	(None)	0	0.03
$m_{i,c}$	(None)	0	0.03
$V_1$	$\mu\text{m}^3 \mu\text{m}^{-2}$	0	0.14
$V_2$	$\mu\text{m}^3 \mu\text{m}^{-2}$	0	0.11
$V_3$	$\mu\text{m}^3 \mu\text{m}^{-2}$	0	0.07
$V_4$	$\mu\text{m}^3 \mu\text{m}^{-2}$	0	0.2
$V_5$	$\mu\text{m}^3 \mu\text{m}^{-2}$	0	0.62
$z_c$	km	0.1	6.0
$P_s$	mb	950	1050
$w_s$	$\text{m s}^{-1}$	0.5	15
Chl $a$	$\text{mg m}^{-3}$	0.01	10

densities (one for each submode), four independent parameters for the fine and coarse real and imaginary components of refractive indices, and one for ALH. Polarimetric single-scattering properties are modeled from these aerosol properties using the Lorenz–Mie code on spherical particles developed by Mishchenko et al. (2002). Note that particle nonsphericity is important for the realistic simulation of mineral dust aerosols (Dubovik et al., 2006) and will be incorporated in the next version of NN forward model following the same approach presented in this study.

The optical model for the underlying water surface is summarized in Gao et al. (2019); briefly, it uses an open-ocean model including contributions from seawater, colored dissolved organic matter, and phytoplankton, the latter two of which are parameterized as a function of chlorophyll  $a$  concentration (Chl  $a$ ;  $\text{mg m}^{-3}$ ). The seawater-polarized scattering properties are derived from the measured normalized Mueller matrix (Voss and Fry, 1984; Kokhanovsky, 2003). The ocean surface roughness is modeled by the isotropic Cox–Munk model with a scalar wind speed (Cox and Munk, 1954). Whitecaps are considered following the parameterization by wind speed (Koepke, 1986). While not done here, for future application to coastal waters where the open-ocean

model is less valid, optimized NN models with sophisticated bio-optical models with seven (Gao et al., 2018) to three (Hannadige et al., 2023) parameters can be developed.

In summary, a total of 17 parameters are used as the input of the NN forward model as indicated in Table 1. These include the 10 aerosol parameters, as well as wind speed, ozone column density, surface pressure, and Chl *a*, and three geometric parameters: the solar zenith angle, viewing zenith angle, and relative azimuth angle.

## 2.3 NN training and performance analysis

The NN forward models (one set for reflectance and one set for DoLP) are trained following the procedures as summarized in Gao et al. (2021a) based on the radiative transfer simulations discussed in the previous section according to the parameter range as summarized in Table 1. This extends the previous work by including ALH and surface pressure as additional parameters, and the range of viewing geometries is also larger than the one used in the airborne measurement by taking advantage of the newly developed IPSS correction (Zhai and Hu, 2022) and the reference frame defined at the Earth's surface (Fig. 1). A total of 10 000 cases of radiative transfer simulations were generated with random values of the input parameters (this set is augmented as described below). A uniform distribution of aerosol optical depth (AOD) in the range between 0.01 and 0.5 is randomly sampled and used to specify volume densities following the sample strategy discussed in Gao et al. (2021a). In this study, we introduce two additional steps in the NN training to boost the NN performance:

1. *Measurement-uncertainty-aware training.* The NN forward models have been shown to achieve much higher accuracy than the HARP measurements using a leaky ReLU (rectified linear unit) activation function and three hidden layers (Gao et al., 2021a). However, at a low wind speed, the sunglint signal, i.e., the sunlight that reflects from the ocean surface around the specular reflection direction, can be strongly peaked, and this can dominate the mean square error (MSE) cost function used by Gao et al. (2021a) for optimization at the expense of precision in other areas. To avoid this issue, the previous study removed simulations close to the direction of specular reflection from the training data set, but the lack of data in sunglint also affected the retrieval results on wind speed and aerosol properties (Gao et al., 2021b). To enable sufficient accuracy to predict the reflection inside and outside of sunglint, we introduce the training cost function that, analogously to the retrieval cost function, normalizes the fitting residuals by

the measurement uncertainty:

$$\chi_{\text{NN},\rho}^2 = \frac{1}{N} \sum_i \left( \frac{[\rho_t(i) - \rho_t^{\text{NN}}(\mathbf{x}; i)]^2}{\sigma_\rho^2(i)} \right), \quad (5)$$

$$\chi_{\text{NN},P}^2 = \frac{1}{N} \sum_i \left( \frac{[P_t(i) - P_t^{\text{NN}}(\mathbf{x}; i)]^2}{\sigma_P^2(i)} \right), \quad (6)$$

where  $\rho_t$  and  $P_t$  indicate training data, and  $\rho_t^{\text{NN}}$  and  $P_t^{\text{NN}}$  indicate the NN predictions.  $N$  in the denominator is the batch size in the training (taken as 1024 here). The same total uncertainty of  $\sigma_\rho = 0.03\rho_t$  and  $\sigma_P = 0.005$  as in Eq. (3) is used here. Therefore,  $\chi_{\text{NN},\rho}^2$  represents the percentage error of the NN predictions, which can effectively incorporate the sunglint signals without directly impacting by its large magnitude. Since a constant value of  $\sigma_P$  is used,  $\chi_{\text{NN},P}^2$  is equivalent to a scaled MSE cost function. The polarization signal is better constrained within 0 and 1 for all viewing geometries, and therefore its training performance is less affected by the sunglint. This new cost function is a convenient and meaningful extension to the conventional MSE cost function applied on a set of normalized training data, especially for reflectance (e.g., Aggarwal, 2018; Fan et al., 2019; Gao et al., 2021a; Aryal et al., 2022; Stamnes et al., 2023). We found that the NN training hyperparameters (such as learning rate or batch size) reported by Gao et al. (2021a) still work well for the new cost function. The resulting training process is aware of the measurement uncertainty and therefore optimizes in a way more relevant to the retrieval's operation.

2. *Training data augmentation.* Generating training data from forward radiative transfer simulations is usually computationally expensive, which limits the NN training performance. However, one RT simulation can be used to generate an arbitrary number of viewing angles and increase the effective training data size, which may improve NN accuracy. This concept is equivalent to data augmentation in machine learning (Shorten and Khoshgoftaar, 2019). Gao et al. (2021a) explored it by sampling 100 sets of random viewing angles from every RT simulation. In this study, we provide a more systematic analysis of such data augmentation by sampling random sets with 100, 400, and 1000 angles, corresponding to total data sizes of 1 million, 4 million, and 10 million points, respectively, from the 10 000 RT simulations.

The NN's training performance is summarized in Fig. 2 for the feed-forward NN architecture with 17 inputs and 4 outputs and various hidden layer sizes (from two layers each with 64 nodes and 128 nodes to three layers each with 128, 256, or 512 nodes). To simplify the notation, we represent the hidden layer structure in a polynomial form; e.g.,  $128^3$  in Fig. 2 represents three hidden layers each with 128 nodes. We

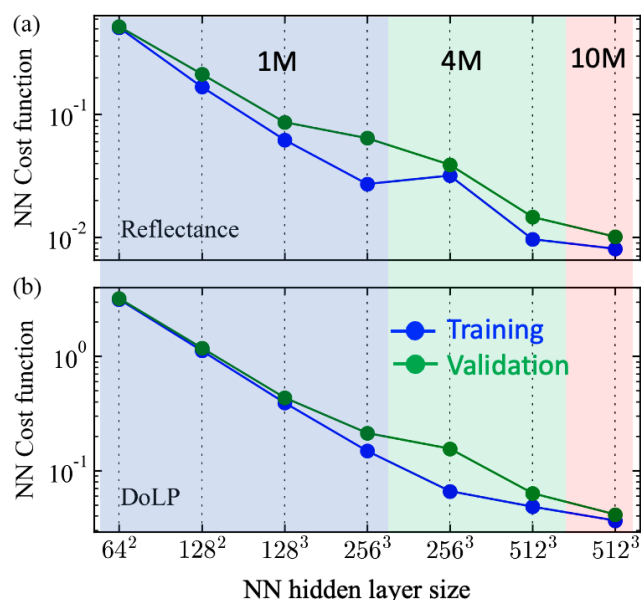


**Figure 2.** Training cost functions for reflectance (a) and DoLP (b) as a function of NN size. The background color indicates the number of training data used: 1 million (blue), 4 million (green), or 10 million (red). The horizontal axis indicates the size of hidden layers, as described in the text; for example,  $64^2$  indicates two hidden layers with 64 nodes at each layer. All the NN models shown here have 17 inputs and 4 outputs.

use 70 % of the simulated data for training (to minimize the training cost function) and the remaining 30 % for validation (to monitor the training process). Figure 2 shows that, with increasing NN hidden layer number and size, the cost functions for both training and validation data decrease, while validation cost eventually becomes larger than training cost. That suggests overfitting for the case of 1 million samples and an NN size of  $128^3$ . Introducing more training data from 4 to 10 million and an NN size up to  $512^3$  further reduces the cost functions to convergence. More training data are generally able to reduce the difference between the training and validation cost function as compared in Fig. 2. Using 10 million total data, the reflectance NN performance stays stable, with a small training cost function value of 0.01, which suggests that the typical fitting residual between the NN and the simulation is about  $\sqrt{0.01} = 0.1$  times the measurement uncertainty, i.e.,  $0.1 \times 3\% = 0.3\%$ .

For DoLP, the NN training is more difficult because the DoLP uncertainty for HARP2 is often much smaller (0.005) than the (3 %) reflectance uncertainty. Figure 2 shows that generally a larger NN size is needed for DoLP to achieve a similar cost function value to reflectance. Using 10 million data and  $512^3$  NN size, the cost function is about 0.04, which suggests that the NN accuracy is  $\sqrt{0.04} = 0.2$  times the measurement uncertainty, with a value of  $0.2 \times 0.005 = 0.001$ . Similar accuracy for NN reflectance requires a size of  $256^3$ . An NN cost function value of 1 would indicate NN accuracy

comparable to the measurement uncertainty, which would be achieved with an NN size of  $64^2$  for reflectance and  $128^2$  for DoLP.

Therefore, for the best performance of applying NN in joint retrieval algorithms, we implemented a two-level cascade scheme in FastMAPOL in which two rounds of retrievals are processed. In the first round, the NN size of  $64^2$  for reflectance and NN size of  $128^2$  for DoLP are used to efficiently find a rough solution. Then in the second (final) round the NN size of  $256^3$  for reflectance and  $512^3$  for DoLP are used to further fine-tune the state vector. Note that each retrieval includes multiple iterations with an order of 10 and involves the use of automatic differentiation to compute the Jacobian matrix analytically (Gao et al., 2021b). Cascading more levels could further improve the performance, but we found that two cascaded levels are sufficient for this study. By comparing the retrieval results with one and two cascading levels, we found that the retrieval uncertainties are similar to each other given the same high-accuracy NNs are used at the last level of retrievals. Therefore, the cascading algorithm will increase retrieval speed without impact retrieval accuracy. To fully test the cascade system as discussed in the next section, we used the best-accuracy NN with the largest size of  $512^3$  to generate a set of synthetic data simulations and performed retrieval with the cascade retrieval scheme.

To further evaluate the NN uncertainty, we generated an additional 1000 independent sets of radiative transfer simulations with realistic HARP geometries as formulated in Gao et al. (2021b) and calculated the mean absolute error (MAE) and RMSE, comparing these simulations to the NN predictions. We found that the MAE is more robust to the impacts of outliers, similar to the discussion on the retrieval uncertainties (Gao et al., 2022). Based on this analysis, discussed in Appendix 1, NN uncertainties are estimated to be 0.5 % for an NN size of  $512^3$  and 0.002 for DoLP using  $512^3$ , both similar to but slightly larger than the estimation from the training cost function. This further confirms that the new training cost function, considering measurement uncertainty, provides an intuitive way to measure the NN optimization. Note that, to ensure the high accuracy of the NN models, the RT simulations with a numerical accuracy much higher than the measurement and NN models are used to generate the training data as discussed in Gao et al. (2021a). For the application to real field measurements, the uncertainties including the NN models, RT simulations, and the measurement uncertainties need to be considered.

### 3 Retrieval analysis on synthetic global over-ocean HARP2 measurements

To evaluate the retrieval performance in terms of both speed and uncertainty in a realistic and representative way, we generated a day of synthetic over-ocean HARP2 measurements along PACE satellite orbits. Random errors based on esti-



mated calibrated uncertainties are added to both the simulated reflectance and DoLP measurements. The retrieval uncertainties are evaluated through error propagation and then validated by comparing the truth and retrieval results based on the Monte Carlo approach (Gao et al., 2022). The viewing and solar geometries are based on realistic satellite orbits. This analysis is useful to understand the retrieval capability of the HARP2 data before PACE's launch.

### 3.1 Synthetic HARP2 L1C radiative transfer simulation

The Level-1C (L1C) file format is used to represent multi-angle measurements where different viewing directions are co-registered on the common spatial location to produce multi-angle measurements for each pixel (Lang et al., 2019). For the PACE mission, a set of common spatial grids are defined within the L1C format for all three instruments: OCI, SPEXone, and HARP2. The grids are based on the swath-based Spacecraft Oblique Cylindrical Equal Area (SOCEA) projection (Snyder, 1987) and documented in the PACE L1C document (Knobelspiesse et al., 2023). The HARP2 data processing will be performed by the PACE Science Data Segment (SDS) following the launch and instrument commissioning. The prelaunch testing of the data processing has been organized around a day in the life (DITL) that has been chosen to be 21 March 2022 (spring equinox), to ensure good daylight coverage over the majority of the world's ocean. The simulated PACE orbit for the DITL has been used to generate the sensor and solar geometry for the instrument data simulations to support the data processing tests by the SDS. The HARP2 simulations and processing results described in the following sections are based on the DITL.

The PACE L1C files are segmented in 5 min granules for daytime portions of the orbit, yielding a total of 165 granules in 15 orbits as shown in Fig. 3. The equatorial crossing time is at 13:00 LT with the satellite ascending northward. The nadir swath width is 1633 km which grows to a maximum swath width of 2380 km around 40° along-track viewing zenith angle. The bin size is 5.2 km. The range of viewing zenith angle can vary from approximately −60 to 60°, with data collected across a time span of 6 min, during which the solar zenith angle can vary by up to 1.5°. Exact per-view solar geometries were used when generating the synthetic HARP2 data, which are important for reducing the impact from the measurement geometries due to satellite motions (Hioki et al., 2021).

In the simulation, the surface pressure, ozone column density, surface wind speed, and speciated aerosol mass concentration vertical profiles are sampled from the NASA GMAO MERRA2 data (Gelaro et al., 2017; Randles et al., 2017; Buchar et al., 2017) along the satellite orbit to best represent the natural global-scale variability in the atmospheric state. Total column effective aerosol microphysical properties (column size and refractive index) were derived from

the MERRA2 simulations of speciated aerosol mass concentration vertical profile by taking a volume-weighted average over the size bins and species in the MERRA2 data set. The aerosol size bins used in MERRA2 are different from the aerosol submodes used in the NN forward model. We have adjusted the volume density and refractive indices of the five aerosol submodes (see Table 1) to best match the aerosol representation in MERRA2. Hygroscopic growth of aerosol size is considered based on the relative humidity profile in the MERRA2 data (Castellanos et al., 2019). The total AOD in MERRA2 data is used to derive the total volume density and ensure that the same AOD will be produced based on the column effective aerosol size, refractive index, and volume density. The monthly average Chl *a* derived from MODIS ocean color products is used as the input to the radiative transfer simulation. Note that there are some small data gaps, most visible in the tropical Atlantic Ocean, due to the gaps in this Chl *a* product from heavy aerosol, cloud, or other data quality flags. However, as they are small, the retrieval performance analysis should not be significantly impacted.

The NN forward model with the maximum accuracy (512<sup>3</sup>) is used to generate the simulated L1C data for a total of 10 million pixels, each with 90 total viewing angles; examples for the HARP2 550 nm band with along-track viewing angles of −43.6, 0.8, and 39.5° are shown in Fig. 3. The newly improved NN forward model can accurately represent the sunglint region, clearly recognizable from large reflectance magnitude at large viewing angles showing in the Northern (a) and Southern Hemisphere (c), as well as near the Equator (b) when looking near the nadir with a smaller reflectance magnitude. At larger viewing angles, prominent polarized signals are also shown in both the Northern (d) and Southern Hemisphere (f). DoLP generally increases with the viewing angle, until approaching the maximum value of 1 at the Brewster angle around 53° at the air–water interface. The backscattering direction usually shows a minimum polarization magnitude, such as near the Equator when looking near the nadir (Fig. 3e).

Two cascaded NN forward models for reflectance and DoLP, respectively, are used to conduct retrievals in the FastMAPOL algorithm as discussed in Sect. 2. The histogram of the cost function values for the first and final retrievals is shown in Fig. 4. The first retrieval, whose NNs have comparable uncertainty to the measurement uncertainty, produces a most probable retrieval cost function of around 2.0. After using the more accurate NN with a much smaller uncertainty, the final retrieval cost functions are mostly close to 1.0. The average total time taken for a retrieval with this two-layer cascade is 0.1 s, as shown in Fig. 4b, compared to 0.2 s for a retrieval using only the higher-accuracy NN (not shown), corresponding to roughly a 50 % speedup.



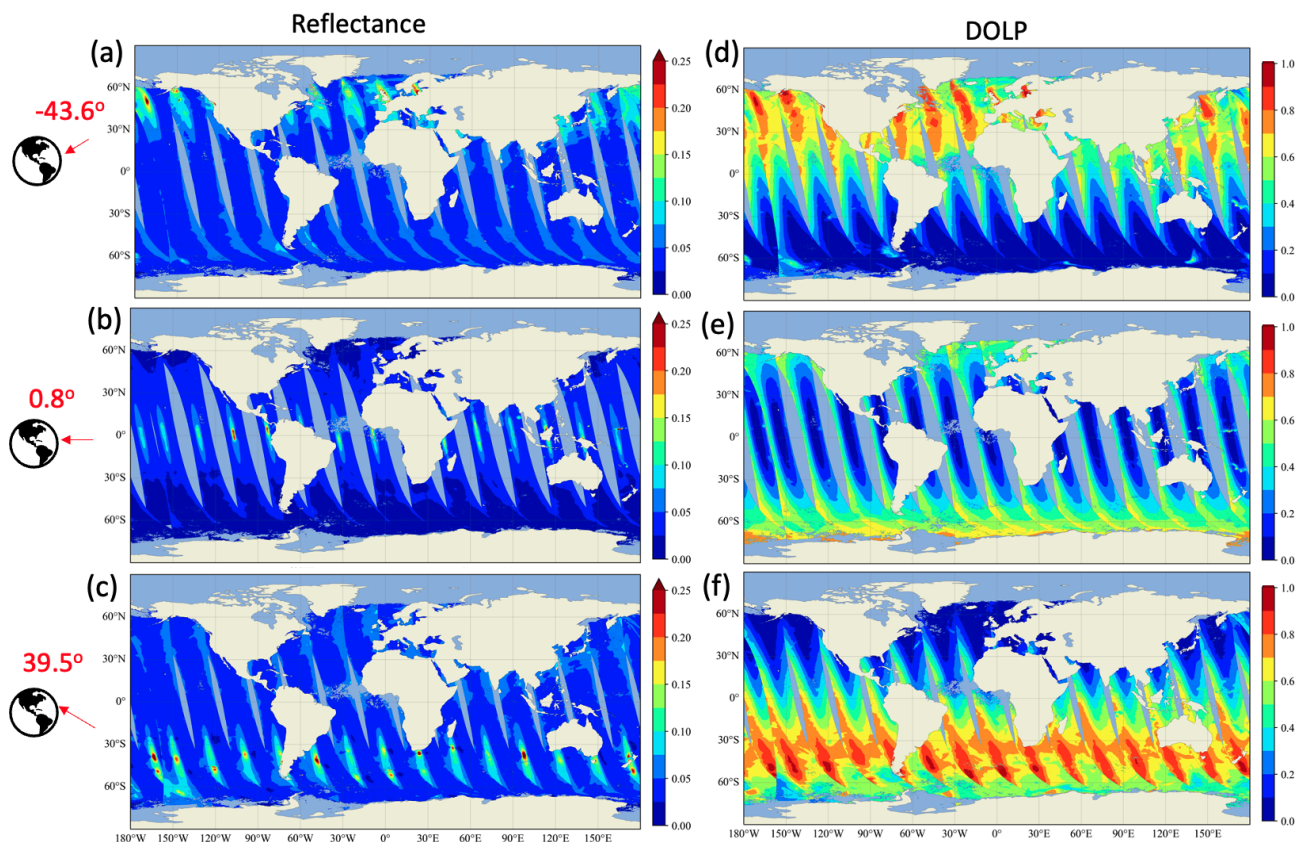


**Figure 3.** Global over-ocean simulation of HARP2 measurements at 550 nm for both reflectance (a–c) and DoLP (d–f), with a total of 15 orbits on the day of 21 March 2022. A total of 90 viewing angles at four HARP2 bands are generated, with three viewing angles in the along-track direction shown in the plots.

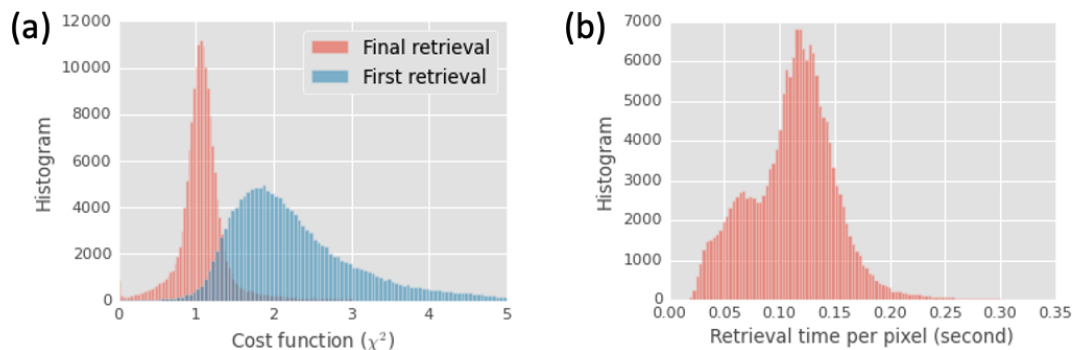


**Figure 4.** (a) Histogram of the cost function values ( $\chi^2$ ) for the first retrieval using a smaller neural network (blue) and the final retrieval using the larger neural network (red) as summarized in Sect. 2. A histogram of processing time for the two-stage process is shown in (b).

### 3.2 Retrieval results

Initially, we conducted a retrieval analysis on a subset of data by including all the parameters as shown in Table 1 except the three geometric variables. The retrieval uncertainties for the ozone density and surface pressure are large, with an MAE of 53 DU and 24 mb and an RMSE value of 69 DU and 32 mb, respectively. As a result, instead of retrieving

these two parameters, we choose to use the value directly from MERRA2 and retrieve only aerosol and ocean properties (which also results in slightly increased accuracy) when applying FastMAPOL to the L1C simulated data. Besides the directly retrieved quantities (Table 1), the aerosol optical depth (AOD) and single-scattering albedo (SSA) for both the fine and coarse modes were computed from retrieved aerosol volume densities and refractive indices using corresponding

NNs trained similarly to the reflectance and DoLP but with a much smaller size of two hidden layers each with 64 nodes (Gao et al., 2021a). Total AOD is obtained as the summation of the fine- and coarse-mode AODs. Effective radius and variance are also calculated from the components' sizes and retrieved volumes.

Figure 5 shows the global map of the retrieved AOD and ALH as well as the corresponding truth values and the retrieval uncertainties based on error propagation. The retrieval value and truth values are very similar to each other as shown in Fig. 5a and b for AOD. Larger uncertainties are mostly associated with the edge of the orbit, where fewer than five viewing angles per band (or total 20–30 angles) are available (see also the analysis in Hasekamp and Landgraf, 2007; Wu et al., 2015; Xu et al., 2017; Gao et al., 2021b). For real PACE data, the adaptive data screening method will be used to automatically remove the angles impacted by cirrus clouds and anomalies, and therefore the uncertainties will depend on the number of available angles associated with the location and size of those clouds (Gao et al., 2021b). Figure 5e and d show that the aerosol layer height (ALH) error has a stronger dependency on the AOD, with performance being generally better (and uncertainties smaller) where AOD is larger.

Data densities showing the correlation and difference between retrieval and truth are shown for AOD, ALH, fine-mode volume fraction (fvf), wind speed, and Chl *a* in Fig. 6. The retrievals perform well, with the RMSE for AOD, ALH, fvf, wind speed, and  $\log_{10}(\text{Chl } a)$  of 0.011, 0.9 km, 0.06,  $1.4 \text{ m s}^{-1}$ , and 0.19, respectively. Similar to Fig. 6, Fig. 7 shows the comparison between the retrieval results, with the truth for the fine-mode AOD at 550 nm, real part of the refractive index, single-scattering albedo, effective radius, and variance. The difference between retrieval and truth seems to strongly depend on the fine-mode aerosol loading as shown in the second row of Fig. 7. However, the retrieval becomes more challenging for the coarse mode as shown in Fig. 8 due to the much lower coarse AOD in general.

### 3.2.1 Uncertainty analysis

To understand the quality of the retrieval products, “theoretical retrieval uncertainties” are evaluated from the error propagation method which maps the measurement uncertainties to the retrieval domain based on the Jacobian with converged retrieval parameters (Rodgers, 2000) and accelerated using NN automatic differentiation (Gao et al., 2021b). This uncertainty can be evaluated at every pixel and therefore provide a flexible metric to evaluate retrieval quality. Examples of AOD and ALH uncertainties are shown in Fig. 6c and f. However, the real retrieval quality also depends on how well the retrieval converges, which can eventually be evaluated based on the difference between the retrieval results and the truth as shown in Figs. 6–8. To verify that the theoretical retrieval uncertainty represents actual retrieval results, we employ the Monte Carlo error propagation (MCEP)

method, which generates random samples of errors based on the theoretical uncertainties. Then, the histogram of the random errors for a large volume of data can be compared with the distribution of the real error (difference between retrieval and truth) so that we can assess the difference and similarity of error distribution derived from the two methods (Gao et al., 2022).

We further group all the pixels according to their AOD values in steps of 0.01 based on the retrieval results shown in Figs. 6–8. The mean absolute error (MAE) is used to evaluate both the average theoretical and real uncertainties, with results summarized in Fig. 9. Figure 9a1 shows that both the theoretical (red lines) and the true (blue lines) absolute uncertainties of AOD increase from 0.002–0.004 to 0.015 as AOD increases from 0.01 to 0.45, which also corresponds to the reduction of relative uncertainty from 20 %–40 % to 5 %. The results agree with the analysis on synthetic HARP2 measurements with a uniform distribution of AOD (Gao et al., 2021b, 2022). Points with AOD > 0.45 are excluded because there are a small number of pixels in this range so that a few outliers could affect the statistics significantly. The high-quality AOD may be useful for climate studies which usually require a goal uncertainty of less than 0.02 (Mishchenko et al., 2004; Kahn, 2015; GCOS, 2022).

Uncertainties of ALH decrease from 1 to 0.5 km within the range of AOD for both theoretical and real uncertainty. The retrieval uncertainty is larger than the results from the RSP instrument, using a spectral range of 410–1590 nm, where the MAE between the true the retrieval values is less than 250 m (Wu et al., 2016), probably as HARP2's shortest wavelength is 440 nm, and it has a larger polarimetric uncertainty of 0.005 compared with RSP (0.002). However, the ALH can still be useful for radiative forcing studies (e.g., Jia et al., 2022) and air quality investigations (e.g., Wang and Christopher, 2003).

Due to the wide angular range and the inclusion of sunglint signals in the NN forward model, the real wind speed accuracy is found to be much higher ( $1 \text{ m s}^{-1}$ ) compared to previous studies of 2–3  $\text{m s}^{-1}$  (Gao et al., 2022). The theoretical uncertainty has a smaller value of around  $0.5 \text{ m s}^{-1}$ , which suggests further room for retrieval improvement. The Chl *a* uncertainties are evaluated as the MAE of the  $\log_{10}(\text{Chl } a)$  uncertainty, as recommended by Seegers et al. (2018):

$\text{MAE}(\log) = 10^Y$ , where

$$Y = \frac{1}{N} \sum_{i=1}^N |\log_{10}(R_i) - \log_{10}(T_i)|, \quad (7)$$

where  $R_i$  and  $T_i$  denote the retrieval and truth values. This “multiplicative error” is a relative, dimensionless metric and takes values of 1 or more, where 1 indicates no error, 1.5 indicates a 50 % error, and so on. Figure 9e1 shows that Chl *a* can be retrieved accurately with a ratio of mostly less than 2.0, which suggests the potential of the MAP data for the evaluation of ocean properties. However, this will become

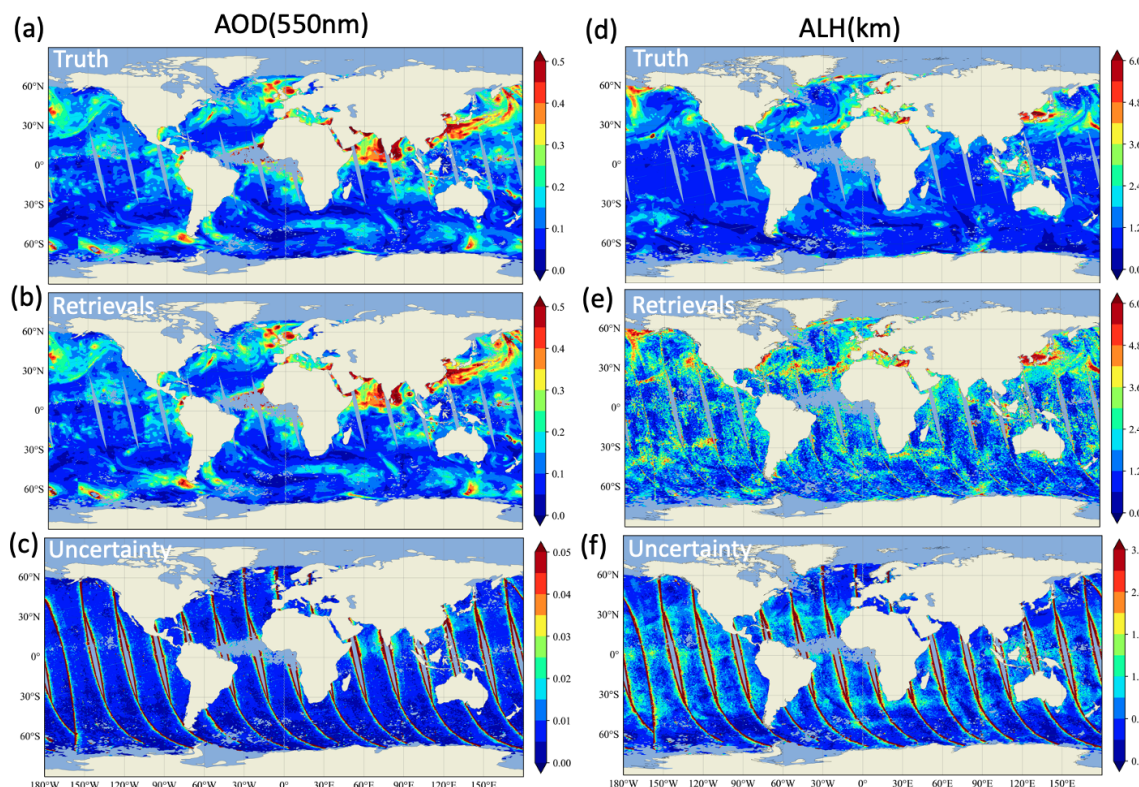


**Figure 5.** The retrieval results, truth, and uncertainties for AOD at 550 nm (a–c) and ALH (d–f).

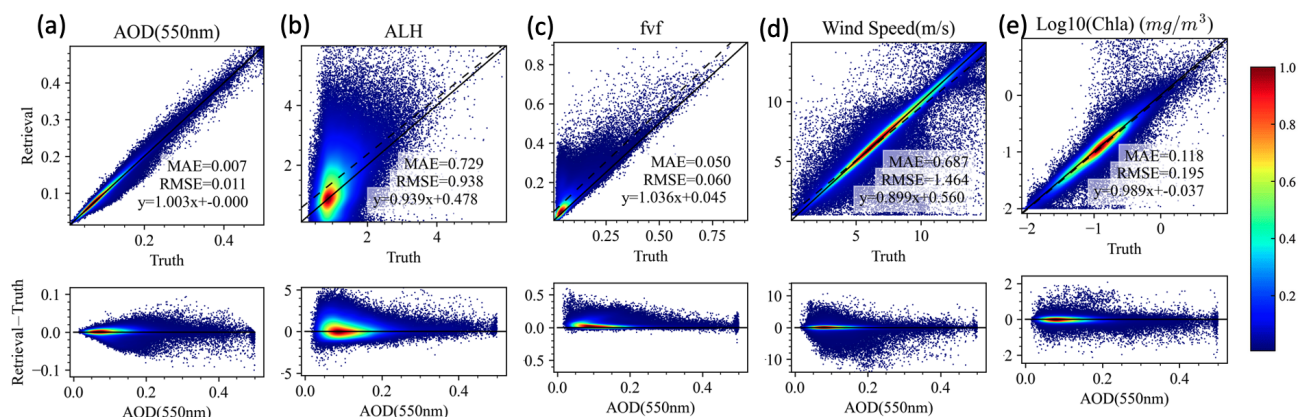


**Figure 6.** The comparisons of the retrieved and truth values for total AOD (550 nm), ALH, fine-mode volume fraction (fvf) wind speed, and Chl *a*. The top row shows heat maps (including the MAE and RMSE), while the bottom row shows the error of the corresponding upper-panel parameters as a function of the total AOD at 550 nm. The colors indicate the data density estimated by a kernel density method (Silverman, 1986).

challenging when the ocean water optical properties are more complex (Gao et al., 2019). Larger differences between the theoretical and real uncertainties are found mostly at  $\text{AOD} > 0.2$ , as the ocean signal becomes increasingly obscured by the aerosols.

For the fine mode, theoretical and real uncertainties are compared in Fig. 9a2–e2. Fine-mode AOD seems to perform similarly to total AOD. The theoretical uncertainties agree

with the real uncertainties when fine-mode AOD is larger than 0.1 but underestimate real uncertainties when AOD is lower. This may indicate lower sensitivity and higher instability due to the impacts of local minima in cost functions. However, the theoretical uncertainty seems to capture the real uncertainty well for effective radius and variance across the range of fine-mode AOD.



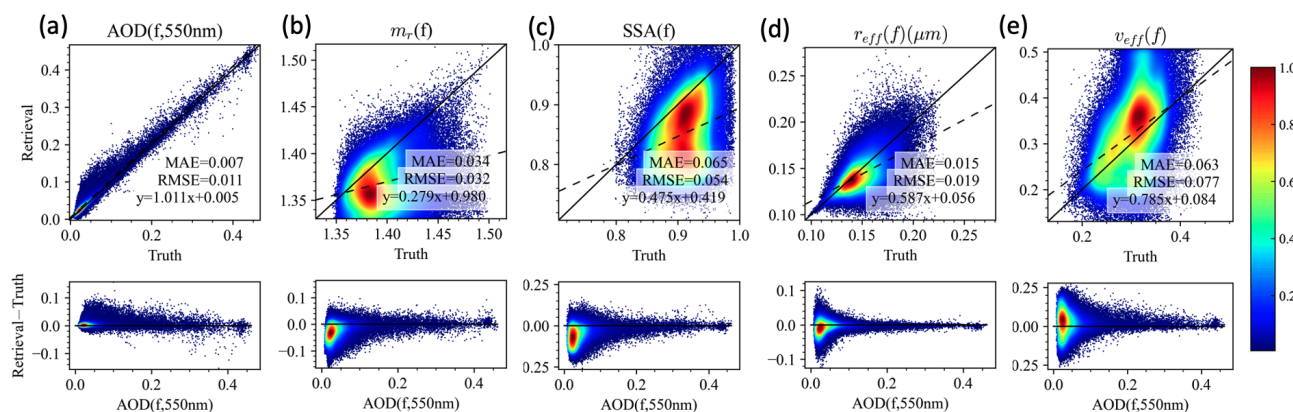


**Figure 7.** As in Fig. 6 except for fine-mode AOD, refractive index ( $m_r$ ), SSA, effective radius ( $r_{eff}$ ), and variance ( $v_{eff}$ ) and the bottom row as a function of fine-mode AOD.

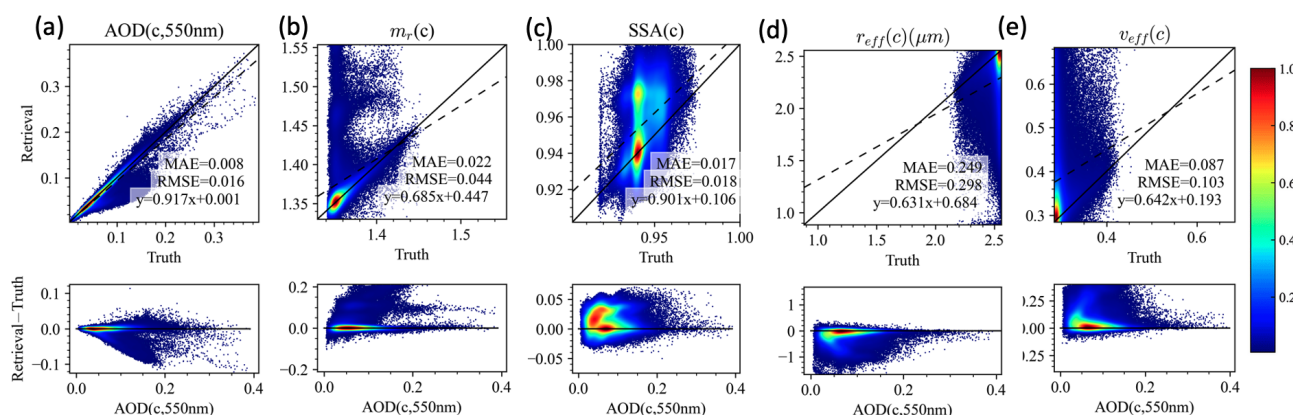


**Figure 8.** As in Fig. 7 except for coarse-mode properties instead of fine mode.

For the coarse mode, as the range of the coarse-mode imaginary refractive index in MERRA2 is limited (mostly  $< 0.001$ , probably due to the dominance of sea salt or other coarse soluble aerosols), we limited the retrieval of this parameter to a similar range. The large spread of retrieved SSA in Fig. 8c suggests the lack of sensitivity on the retrieval of the coarse-mode imaginary refractive index. The uncertainties are captured well by the theoretical uncertainties in Fig. 9c3. After launch, sensitivity studies will be required to better prescribe the coarse-mode imaginary refractive index. From the current synthetic data analysis, the real uncertainties are much higher than the theoretical uncertainties for coarse-mode properties. Low sensitivity is expected due to the low aerosol loading and lack of longer-wavelength short-wave infrared (SWIR) bands and therefore the challenges to converge to the global minimum of the cost function. The real uncertainties on coarse AOD are much larger than the fine-mode uncertainties with a value of up to 0.03, although the theoretical uncertainty for coarse-mode AOD is smaller (0.002–0.005) than the fine-mode AOD uncertainty (0.005–0.015), possibly due to the stronger constraint on the coarse-mode absorption. For PACE data, a future synergy with the

SWIR bands from OCI may be used to improve the coarse-mode retrieval quality (Hasekamp et al., 2019). However, the impact of the coarse-mode aerosols in the application of atmospheric correction may be less severe due to their small overall value and weak spectral variation.

#### 4 Discussion and conclusions

In this study we illustrated the advancements made to the FastMAPOL retrieval algorithm, including various improvements in the radiative transfer model, NN training methodology, NN architecture, and retrieval scheme.

- *Radiative transfer model.* We improved the radiative transfer model which is used to generate the training data for spaceborne measurement by including spherical shell correction, realistic solar and viewing geometries, and additional input parameters such as surface pressure and aerosol layer height.
- *Training methodology.* The NN models are trained by incorporating the measurement uncertainty model

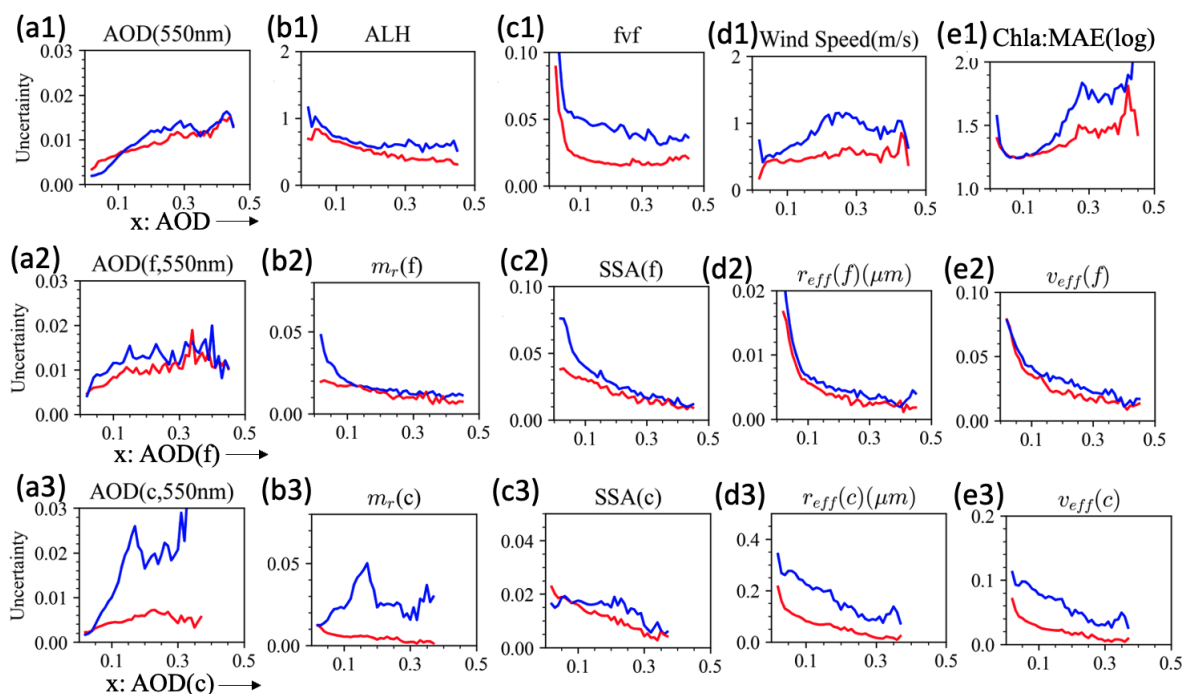


**Figure 9.** Comparison of theoretical (red) and real retrieval uncertainties (blue) as a function of AOD for AOD, SSA, real part of the refractive index ( $m_r$ ), effective radius ( $r_{\text{eff}}$ ) and variance ( $v_{\text{eff}}$ ), wind speed, and Chl *a*. AOD, fine-mode AOD, and coarse-mode AOD values are used at the  $x$  axis from 0.01 to 0.45 with a step of 0.01.

into the training cost function, which better represents sunglint signals and helps improve the NN relevance to the retrieval's operation.

- *NN architecture.* Flexible NN models with various numbers of hidden layers and numbers of nodes are investigated, which achieve different speeds and accuracies.
- *Retrieval scheme.* Two levels of NN models with increasing sizes and accuracies are used in a cascading retrieval scheme to achieve high retrieval efficiency and performance.

With the improved NN models and retrieval schemes, we also systematically investigate the retrievability of aerosol and ocean parameters and their uncertainty. The retrieval uncertainties are analyzed based on the FastMAPOL retrievals on the synthetic data sets, including the aerosol optical properties such as AOD and SSA and microphysical properties including aerosol size, refractive index, and height with more realistic statistics of the parameter values and viewing and solar geometries. For example, the overall uncertainties for AOD and wind speed are 0.01 and  $1.4 \text{ m s}^{-1}$ . The retrieval uncertainties at the pixel level are shown to depend on the number of available viewing angles and the aerosol loading. Fine-mode aerosol properties, such as the aerosol refractive index, generally show smaller retrieval uncertainties and better agreement between error propagation uncertainties and real uncertainties from simulated retrievals. Coarse-

mode aerosol retrieval uncertainties are larger and not fully captured by error propagations. We also demonstrated that HARP2 measurements can be used to derive aerosol layer height with an uncertainty of 0.5 to 1.0 km depending on the aerosol loading.

Regarding the retrieval speed, in a previous version of the FastMAPOL algorithm we employed NN forward models with analytical Jacobian evaluation based on automatic differentiation, which had expedited the processing of the AirHARP data from 1 h per pixel using on-the-fly radiative transfer forward model simulations to around 0.3 s per pixel (Gao et al., 2021a, b). In this study, the processing speed of the HARP2 synthetic data is further improved to about 0.2 s per pixel by optimizing the numerical code. It is further reduced to 0.1 s using a single CPU core by applying a cascaded approach in FastMAPOL. With the newest development, the speed to process a single PACE LIC 5 min granule with an order of  $400 \times 500$  pixels can be finished within 5 h in a single CPU core. As already demonstrated in our system, the whole day of synthetic data was processed within 5 h by utilizing distributed computing and running all granules parallelly. This illustrates that global-scale MAP data processing is feasible.

Furthermore, additional ocean properties can be derived from the MAP measurements and retrieval results. For example, NN models based on the retrieved aerosol and ocean parameters have been used to obtain water-leaving sig-

nals through the atmospheric and BRDF (bidirectional reflectance distribution function) corrections on real or synthetic AirHARP and HARP2 measurements (Gao et al., 2021a, 2022). Similarly, the retrieved aerosol properties can be used to assist the hyperspectral atmospheric correction as demonstrated using SPEX data as a PACE OCI proxy (Gao et al., 2019; Hannadige et al., 2021). NN methods can also be used to predict the polarimetric reflectance associated with complex water optical properties (Mukherjee et al., 2020) and instantaneous photosynthetically available radiation models within ocean bodies (Aryal et al., 2022) and derive in-water optical properties from top-of-atmosphere MAP measurements for PACE (Agagliate et al., 2023).

Therefore, based on the improved NN forward models, this study provided an efficient spaceborne MAP data processing algorithm and discussed the data product and the associated uncertainties analyzed from a global-scale synthetic HARP2 data set. For the future applications to the real satellite data after PACE launch, it would be important to ensure the forward model is appropriate for the measurements by conducting input data quality control and data screening (Gao et al., 2021b). Further evaluations on the measurement uncertainty model can be conducted by comparing it with fitting residual statistics (Gao et al., 2023). The algorithm and uncertainty analysis provide a viable way to process global HARP2 data and improve our capability to observe, understand, and protect our environment.

## Appendix A: Evaluation of NN forward model uncertainty

As discussed in Sect. 2, to evaluate the NN uncertainty independently, we use an additional set of 1000 simulations with realistic HARP geometries, formulated by Gao et al. (2021b). To further evaluate the accuracy of the NN, both the mean absolute error (MAE) and the root mean square error (RMSE) are computed for both reflectance and DoLP as shown in Fig. A1 and Table A1. As discussed in Gao et al. (2022), the MAE is more robust than the RMSE to outliers. We estimate the NN uncertainties using the MAE as  $\sigma_{\text{NN}} = \pi/2 \times \text{MAE}$ , which is equivalent to assuming the error following a Gaussian distribution (Gao et al., 2022). Note that the RMSE is slightly larger than  $\sigma_{\text{NN}}$ . The estimated errors are similar to the results obtained in Gao et al. (2021a), where 20 000 training data each sampled with 100 angles are used. Here, we decreased the training data set to 10 000 but sampled each case at 1000 angles. Note that in this study we have included the angles with sunglint, which includes many more cases in the uncertainty evaluations. To further improve the accuracy, we need to increase both the NN size and training data volume. A balance of training data volume, NN speed (smaller size), and NN accuracy (larger size, larger training data volume) is discussed in Sect. 2. NN accuracy is estimated with a value of 0.5 % for an NN size of  $512^3$  and a value of 0.002 for DoLP using  $512^3$ ; both are slightly larger than the estimation from the training cost function but on a similar scale as discussed in Sect. 2. The estimated NN uncertainties can be included in the total uncertainty model in the retrieval cost function as discussed by Gao et al. (2021a).

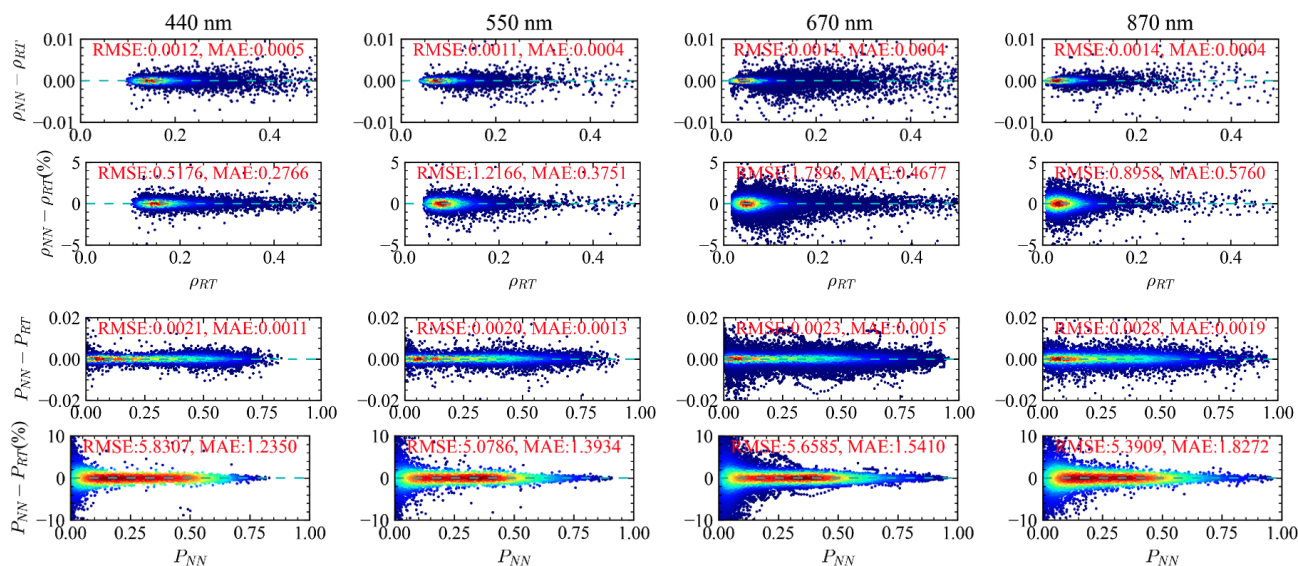


**Figure A1.** Comparison between the radiative transfer simulation and NN prediction: the left panel is reflectance ( $\rho$ ) and the right panel is DoLP ( $P$ ). The scatter plots are shown in the top panel, the absolute different in the middle panel, and the percentage difference in the bottom panel. For each plot, the data points for the 550, 660, and 870 nm bands are shifted upward by constant offsets consecutively, as indicated by the solid cyan lines.

**Table A1.** Comparisons of the uncertainties for reflectance ( $\rho$ ) and DoLP ( $P$ ) for both measurements and forward models including calibration uncertainty ( $\sigma_{\text{cal}}$ ), the radiative transfer simulation uncertainty ( $\sigma_{\text{RT}}$ ), and the NN uncertainty ( $\sigma_{\text{NN}}$ ). The percentage values listed in the table indicate the percentage uncertainties.

Quantities	Uncertainties	440 nm	550 nm	670 nm	870 nm
$\rho_t$	$\sigma_{\text{cal}}$	3 %	3 %	3 %	3 %
	$\sigma_{\text{RT}}$	0.00012 (0.08 %)	0.00005 (0.07 %)	0.00010 (0.2 %)	0.00015 (0.4 %)
	RMSE <sub>NN</sub>	0.0012 (0.52 %)	0.0011 (1.22 %)	0.0014 (1.79 %)	0.0014 (0.90 %)
	MAE <sub>NN</sub>	0.0005 (0.28 %)	0.0004 (0.38 %)	0.0004 (0.47 %)	0.0004 (0.58 %)
	$\sigma_{\text{NN}}$	0.0007 (0.35 %)	0.0005 (0.47 %)	0.0005 (0.59 %)	0.0005 (0.72 %)
$P_t$	$\sigma_{\text{cal}}$	0.005	0.005	0.005	0.005
	$\sigma_{\text{RT}}$	0.0002	0.0002	0.0005	0.0007
	RMSE <sub>NN</sub>	0.0021	0.0020	0.0023	0.0028
	MAE <sub>NN</sub>	0.0011	0.0013	0.0015	0.0019
	$\sigma_{\text{NN}}$	0.0014	0.0016	0.0018	0.0023



**Data availability.** The relevant data for this study can be accessed from NASA's Ocean Biology Distributed Active Archive Center (OB.DAAC) as follows: PACE L1C spatial grids, <https://oceandata.sci.gsfc.nasa.gov/directdataaccess/Level-1C/PACE-spacecraft/2022/080/> (OB.DAAC, 2023a); ancillary data, <https://oceandata.sci.gsfc.nasa.gov/directdataaccess/Ancillary/PACE-spacecraft/2022/080/> (OB.DAAC, 2023b); HARP2 L1C simulated data, <https://oceandata.sci.gsfc.nasa.gov/directdataaccess/Level-1C/PACE-HARP2/2022/080/> (OB.DAAC, 2023c); and HARP2 L2 FastMAPOL product, <https://oceandata.sci.gsfc.nasa.gov/directdataaccess/Level-2/PACE-HARP2/2022/080/> (OB.DAAC, 2023d). Note that additional updates mostly related to ancillary data (Chl *a*) coverage, HARP2 swath width and viewing geometry are included in these datasets.

**Author contributions.** MG, BAF, and KK formulated the study concept. MG generated the scientific data and wrote the original paper. PWZ developed the radiative transfer model with support from NH. XX, AP, and JVM provided and advised on the HARP data. FP, BAF, and PJW advised on the algorithm testing process. PC provided and advised on the MERRA2 data and tables. AMS, AI, GF, OH, YH, and BC advised on the inversion and uncertainty methodologies. All authors provided critical feedback and edited the paper.

**Competing interests.** At least one of the (co-)authors is a member of the editorial board of *Atmospheric Measurement Techniques*. The peer-review process was guided by an independent editor, and the authors also have no other competing interests to declare.

**Disclaimer.** Publisher's note: Copernicus Publications remains neutral with regard to jurisdictional claims made in the text, published maps, institutional affiliations, or any other geographical representation in this paper. While Copernicus Publications makes every effort to include appropriate place names, the final responsibility lies with the authors.

**Acknowledgements.** The authors would like to thank Joel Gales, Wayne Roberson, and Sean Foley for the support and discussions; the Ocean Biology Processing Group (OBPG) system team for the support in high-performance computing (HPC); and Carina Poulin for designing the FastMAPOL logo.

**Financial support.** Meng Gao, Bryan A. Franz, Kirk Knobel-spie, Brian Cairns, Amir Ibrahim, Frederick Patt, Andrew M. Sayer, and P. Jeremy Werdell have been supported by the NASA PACE project. Peng-Wang Zhai recognizes the support from the PACE Science and Application Team (NASA grants (grant no. 80NSSC20M0227)).

**Review statement.** This paper was edited by Meng Gao and reviewed by two anonymous referees.

## References

- Agagliate, J., Foster, R., Ibrahim, A., and Gilerson, A.: A neural network approach to the estimation of in-water attenuation to absorption ratios from PACE mission measurements, *Frontiers in Remote Sensing*, 4, 1–20, <https://doi.org/10.3389/frsen.2023.1060908>, 2023.
- Aggarwal, C. C.: *Neural Networks and Deep Learning: A Textbook*, Springer, Cham, Switzerland, ISBN 3319944622, 2018.
- Anderson, G., Clough, S., Kneizys, F., Chetwynd, J., and Shettle, E.: *AFGL Atmospheric Constituent Profiles (0.120 km)*, Air Force Geophysics Lab., Hanscom AFB, MA (USA), AFGL-TR-86-0110, 1986.
- Aryal, K., Zhai, P.-W., Gao, M., and Franz, B. A.: Instantaneous photosynthetically available radiation models for ocean waters using neural networks, *Appl. Opt.*, 61, 9985–9995, <https://doi.org/10.1364/AO.474914>, 2022.
- Baydin, A. G., Pearlmutter, B. A., Radul, A. A., and Siskind, J. M.: Automatic differentiation in machine learning: a survey, *J. Mach. Learn. Res.*, 18, 1–43, 2018.
- Branch, M. A., Coleman, T. F., and Li, Y.: A Subspace, Interior, and Conjugate Gradient Method for Large-Scale Bound-Constrained Minimization Problems, *SIAM J. Sci. Comput.*, 21, 1–23, <https://doi.org/10.1137/S1064827595289108>, 1999.
- Buchard, V., Randles, C. A., da Silva, A. M., Darmenov, A., Colarco, P. R., Govindaraju, R., Ferrare, R., Hair, J., Beyersdorf, A. J., Ziemba, L. D., and Yu, H.: The MERRA-2 Aerosol Reanalysis, 1980 Onward. Part II: Evaluation and Case Studies, *J. Climate*, 30, 6851–6872, <https://doi.org/10.1175/JCLI-D-16-0613.1>, 2017.
- Cairns, B., Russell, E. E., and Travis, L. D.: Research Scanning Polarimeter: calibration and ground-based measurements, *Proc. SPIE*, 3754, 186–196, <https://doi.org/10.1117/12.366329>, 1999.
- Castellanos, P., Da Silva, A. M., Darmenov, A. S., Buchard, V., Govindaraju, R. C., Ciren, P., and Kondragunta, S.: A Geostationary Instrument Simulator for Aerosol Observing System Simulation Experiments, *Atmosphere*, 10, 1–36, <https://doi.org/10.3390/atmos10010002>, 2019.
- Chen, C., Dubovik, O., Fuertes, D., Litvinov, P., Lapyonok, T., Lopatin, A., Ducos, F., Derimian, Y., Herman, M., Tanré, D., Remmer, L. A., Lyapustin, A., Sayer, A. M., Levy, R. C., Hsu, N. C., Descloîtres, J., Li, L., Torres, B., Karol, Y., Herrera, M., Herreras, M., Aspörsberger, M., Wanzelboeck, M., Bindreiter, L., Marth, D., Hanger, A., and Federspiel, C.: Validation of GRASP algorithm product from POLDER/PARASOL data and assessment of multi-angular polarimetry potential for aerosol monitoring, *Earth Syst. Sci. Data*, 12, 3573–3620, <https://doi.org/10.5194/essd-12-3573-2020>, 2020.
- Chen, C., Dubovik, O., Schuster, G. L., Chin, M., Henze, D. K., Lapyonok, T., Li, Z., Derimian, Y., and Zhang, Y.: Multi-angular polarimetric remote sensing to pinpoint global aerosol absorption and direct radiative forcing, *Nat. Commun.*, 13, 7459, <https://doi.org/10.1038/s41467-022-35147-y>, 2022.
- Chen, N., Li, W., Gatebe, C., Tanikawa, T., Hori, M., Shimada, R., Aoki, T., and Stamnes, K.: New neural network cloud mask algorithm based on radiative transfer simulations, *Remote Sens. Environ.*, 219, 62–71, <https://doi.org/10.1016/j.rse.2018.09.029>, 2018.
- Chowdhary, J., Cairns, B., Mishchenko, M. I., Hobbs, P. V., Cota, G. F., Redemann, J., Rutledge, K., Holben, B. N., and Rus-

- sell, E.: Retrieval of Aerosol Scattering and Absorption Properties from Photopolarimetric Observations over the Ocean during the CLAMS Experiment, *J. Atmos. Sci.*, 62, 1093–1117, <https://doi.org/10.1175/JAS3389.1>, 2005.
- Cox, C. and Munk, W.: Measurement of the Roughness of the Sea Surface from Photographs of the Sun's Glitter, *J. Opt. Soc. Am.*, 44, 838–850, 1954.
- Di Noia, A., Hasekamp, O. P., van Harten, G., Rietjens, J. H. H., Smit, J. M., Snik, F., Henzing, J. S., de Boer, J., Keller, C. U., and Volten, H.: Use of neural networks in ground-based aerosol retrievals from multi-angle spectropolarimetric observations, *Atmos. Meas. Tech.*, 8, 281–299, <https://doi.org/10.5194/amt-8-281-2015>, 2015.
- Diego, G. and Loyola, R.: Using neural network ensembles for the operational retrieval of ozone total columns, in: IGARSS 2004. 2004 IEEE International Geoscience and Remote Sensing Symposium, Alaska, USA, 20–24 September 2004, Vol. 2, 1041–1044, <https://doi.org/10.1109/IGARSS.2004.1368589>, 2004.
- Diner, D. J., Boland, S. W., Brauer, M., Bruegge, C., Burke, K. A., Chipman, R., Girolamo, L. D., Garay, M. J., Hasheminassab, S., Hyer, E., Jerrett, M., Jovanovic, V., Kalashnikova, O. V., Liu, Y., Lyapustin, A. I., Martin, R. V., Nastan, A., Ostro, B. D., Ritz, B., Schwartz, J., Wang, J., and Xu, F.: Advances in multiangle satellite remote sensing of speciated airborne particulate matter and association with adverse health effects: from MISR to MAIA, *J. Appl. Remote Sens.*, 12, 1–22, <https://doi.org/10.1117/1.JRS.12.042603>, 2018.
- Duan, M., Min, Q., and Li, J.: A fast radiative transfer model for simulating high-resolution absorption bands, *J. Geophys. Res.-Atmos.*, 110, D15201, <https://doi.org/10.1029/2004JD005590>, 2005.
- Dubovik, O., Sinyuk, A., Lapyonok, T., Holben, B. N., Mishchenko, M., Yang, P., Eck, T. F., Volten, H., Muñoz, O., Veihelmann, B., van der Zande, W. J., Leon, J.-F., Sorokin, M., and Slutsker, I.: Application of spheroid models to account for aerosol particle nonsphericity in remote sensing of desert dust, *J. Geophys. Res.-Atmos.*, 111, D11208, <https://doi.org/10.1029/2005JD006619>, 2006.
- Dubovik, O., Herman, M., Holdak, A., Lapyonok, T., Tanré, D., Deuzé, J. L., Ducos, F., Sinyuk, A., and Lopatin, A.: Statistically optimized inversion algorithm for enhanced retrieval of aerosol properties from spectral multi-angle polarimetric satellite observations, *Atmos. Meas. Tech.*, 4, 975–1018, <https://doi.org/10.5194/amt-4-975-2011>, 2011.
- Dubovik, O., Lapyonok, T., Litvinov, P., Herman, M., Fuertes, D., Ducos, F., Lopatin, A., Chaikovskiy, A., Torres, B., Derimian, Y., Huang, X., Aspörsberger, M., and Federspiel, C.: GRASP: a versatile algorithm for characterizing the atmosphere, *SPIE Newsroom*, 1–4 pp., <https://doi.org/10.1117/2.1201408.005558>, 2014.
- Dubovik, O., Li, Z., Mishchenko, M. I., Tanré, D., Karol, Y., Bojkov, B., Cairns, B., Diner, D. J., Espinosa, W. R., Goloub, P., Gu, X., Hasekamp, O., Hong, J., Hou, W., Knobelspiesse, K. D., Landgraf, J., Li, L., Litvinov, P., Liu, Y., Lopatin, A., Marbach, T., Maring, H., Martins, V., Meijer, Y., Milinevsky, G., Mukai, S., Parol, F., Qiao, Y., Remer, L., Rietjens, J., Sano, I., Stammes, P., Stammes, S., Sun, X., Tabary, P., Travis, L. D., Waquet, F., Xu, F., Yan, C., and Yin, D.: Polarimetric remote sensing of atmospheric aerosols: Instruments, methodologies, results, and perspectives, *J. Quant. Spectrosc. Ra.*, 224, 474–511, <https://doi.org/10.1016/j.jqsrt.2018.11.024>, 2019.
- Fan, C., Fu, G., Di Noia, A., Smit, M., Rietjens, J. H., Ferrare, R. A., Burton, S., Li, Z., and Hasekamp, O. P.: Use of A Neural Network-Based Ocean Body Radiative Transfer Model for Aerosol Retrievals from Multi-Angle Polarimetric Measurements, *Remote Sens.-Basel*, 11, 2877, <https://doi.org/10.3390/rs11232877>, 2019.
- Fan, Y., Li, W., Gatebe, C. K., Jamet, C., Zibordi, G., Schroeder, T., and Stamnes, K.: Atmospheric correction over coastal waters using multilayer neural networks, *Remote Sens. Environ.*, 199, 218–240, 2017.
- Fougnie, B., Marbach, T., Lacan, A., Lang, R., Schlüssel, P., Poli, G., Munro, R., and Couto, A. B.: The multi-viewing multi-channel multi-polarisation imager – Overview of the 3MI polarimetric mission for aerosol and cloud characterization, *J. Quant. Spectrosc. Ra.*, 219, 23–32, <https://doi.org/10.1016/j.jqsrt.2018.07.008>, 2018.
- Frouin, R. J., Franz, B. A., Ibrahim, A., Knobelspiesse, K., Ahmad, Z., Cairns, B., Chowdhary, J., Dierssen, H. M., Tan, J., Dubovik, O., Huang, X., Davis, A. B., Kalashnikova, O., Thompson, D. R., Remer, L. A., Boss, E., Coddington, O., Deschamps, P.-Y., Gao, B.-C., Gross, L., Hasekamp, O., Omar, A., Pelletier, B., Ramon, D., Steinmetz, F., and Zhai, P.-W.: Atmospheric Correction of Satellite Ocean-Color Imagery During the PACE Era, *Front. Earth Sci.*, 7, 145, <https://doi.org/10.3389/feart.2019.00145>, 2019.
- Fu, G. and Hasekamp, O.: Retrieval of aerosol microphysical and optical properties over land using a multimode approach, *Atmos. Meas. Tech.*, 11, 6627–6650, <https://doi.org/10.5194/amt-11-6627-2018>, 2018.
- Fu, G., Hasekamp, O., Rietjens, J., Smit, M., Di Noia, A., Cairns, B., Wasilewski, A., Diner, D., Seidel, F., Xu, F., Knobelspiesse, K., Gao, M., da Silva, A., Burton, S., Hostetler, C., Hair, J., and Ferrare, R.: Aerosol retrievals from different polarimeters during the ACEPOL campaign using a common retrieval algorithm, *Atmos. Meas. Tech.*, 13, 553–573, <https://doi.org/10.5194/amt-13-553-2020>, 2020.
- Gao, M., Zhai, P.-W., Franz, B., Hu, Y., Knobelspiesse, K., Werdell, P. J., Ibrahim, A., Xu, F., and Cairns, B.: Retrieval of aerosol properties and water-leaving reflectance from multi-angular polarimetric measurements over coastal waters, *Opt. Express*, 26, 8968–8989, <https://doi.org/10.1364/OE.26.008968>, 2018.
- Gao, M., Zhai, P.-W., Franz, B. A., Hu, Y., Knobelspiesse, K., Werdell, P. J., Ibrahim, A., Cairns, B., and Chase, A.: Inversion of multiangular polarimetric measurements over open and coastal ocean waters: a joint retrieval algorithm for aerosol and water-leaving radiance properties, *Atmos. Meas. Tech.*, 12, 3921–3941, <https://doi.org/10.5194/amt-12-3921-2019>, 2019.
- Gao, M., Franz, B. A., Knobelspiesse, K., Zhai, P.-W., Martins, V., Burton, S., Cairns, B., Ferrare, R., Gales, J., Hasekamp, O., Hu, Y., Ibrahim, A., McBride, B., Puthukkudy, A., Werdell, P. J., and Xu, X.: Efficient multi-angle polarimetric inversion of aerosols and ocean color powered by a deep neural network forward model, *Atmos. Meas. Tech.*, 14, 4083–4110, <https://doi.org/10.5194/amt-14-4083-2021>, 2021a.
- Gao, M., Knobelspiesse, K., Franz, B. A., Zhai, P.-W., Martins, V., Burton, S. P., Cairns, B., Ferrare, R., Fenn, M. A., Hasekamp, O., Hu, Y., Ibrahim, A., Sayer, A. M., Werdell, P.

- J., and Xu, X.: Adaptive Data Screening for Multi-Angle Polarimetric Aerosol and Ocean Color Remote Sensing Accelerated by Deep Learning, *Frontiers in Remote Sensing*, 2, 46, <https://doi.org/10.3389/frsen.2021.757832>, 2021b.
- Gao, M., Knobelspiesse, K., Franz, B. A., Zhai, P.-W., Sayer, A. M., Ibrahim, A., Cairns, B., Hasekamp, O., Hu, Y., Martins, V., Werdell, P. J., and Xu, X.: Effective uncertainty quantification for multi-angle polarimetric aerosol remote sensing over ocean, *Atmos. Meas. Tech.*, 15, 4859–4879, <https://doi.org/10.5194/amt-15-4859-2022>, 2022.
- Gao, M., Knobelspiesse, K., Franz, B. A., Zhai, P.-W., Cairns, B., Xu, X., and Martins, J. V.: The impact and estimation of uncertainty correlation for multi-angle polarimetric remote sensing of aerosols and ocean color, *Atmos. Meas. Tech.*, 16, 2067–2087, <https://doi.org/10.5194/amt-16-2067-2023>, 2023.
- Gassó, S. and Knobelspiesse, K. D.: Circular polarization in atmospheric aerosols, *Atmos. Chem. Phys.*, 22, 13581–13605, <https://doi.org/10.5194/acp-22-13581-2022>, 2022.
- GCOS: The 2022 GCOS ECVs Requirements (GCOS 245), World Meteorological Organization, 2022.
- Gelaro, R., McCarty, W., Suárez, M. J., Todling, R., Molod, A., Takacs, L., Randles, C. A., Darmenov, A., Bosilovich, M. G., Reichle, R., Wargan, K., Coy, L., Cullather, R., Draper, C., Akella, S., Buchard, V., Conaty, A., da Silva, A. M., Gu, W., Kim, G.-K., Koster, R., Lucchesi, R., Merkova, D., Nielsen, J. E., Parityka, G., Pawson, S., Putman, W., Rienecker, M., Schubert, S. D., Sienkiewicz, M., and Zhao, B.: The Modern-Era Retrospective Analysis for Research and Applications, Version 2 (MERRA-2), *J. Climate*, 30, 5419–5454, <https://doi.org/10.1175/JCLI-D-16-0758.1>, 2017.
- Hannadige, N. K., Zhai, P.-W., Gao, M., Franz, B. A., Hu, Y., Knobelspiesse, K., Werdell, P. J., Ibrahim, A., Cairns, B., and Hasekamp, O. P.: Atmospheric correction over the ocean for hyperspectral radiometers using multi-angle polarimetric retrievals, *Opt. Express*, 29, 4504–4522, <https://doi.org/10.1364/OE.408467>, 2021.
- Hannadige, N. K., Zhai, P.-W., Gao, M., Hu, Y., Werdell, P. J., Knobelspiesse, K., and Cairns, B.: Performance evaluation of three bio-optical models in aerosol and ocean color joint retrievals, *Atmos. Meas. Tech. Discuss.* [preprint], <https://doi.org/10.5194/amt-2023-142>, in review, 2023.
- Hasekamp, O. P. and Landgraf, J.: Linearization of vector radiative transfer with respect to aerosol properties and its use in satellite remote sensing, *J. Geophys. Res.-Atmos.*, 110, D04203, <https://doi.org/10.1029/2004JD005260>, 2005.
- Hasekamp, O. P. and Landgraf, J.: Retrieval of aerosol properties over land surfaces: capabilities of multiple-viewing-angle intensity and polarization measurements, *Appl. Opt.*, 46, 3332–3344, <https://doi.org/10.1364/AO.46.003332>, 2007.
- Hasekamp, O. P., Litvinov, P., and Butz, A.: Aerosol properties over the ocean from PARASOL multiangle photopolarimetric measurements, *J. Geophys. Res.-Oceans*, 116, D14204, <https://doi.org/10.1029/2010JD015469>, 2011.
- Hasekamp, O. P., Fu, G., Rusli, S. P., Wu, L., Noia, A. D., aan de Brugh, J., Landgraf, J., Smit, J. M., Rietjens, J., and van Amerongen, A.: Aerosol measurements by SPEXone on the NASA PACE mission: expected retrieval capabilities, *J. Quant. Spectrosc. Ra.*, 227, 170–184, <https://doi.org/10.1016/j.jqsrt.2019.02.006>, 2019a.
- Hasekamp, O. P., Gryspeerdt, E., and Quaas, J.: Analysis of polarimetric satellite measurements suggests stronger cooling due to aerosol-cloud interactions, *Nat. Commun.*, 10, 5405, <https://doi.org/10.1038/s41467-019-13372-2>, 2019b.
- Hioki, S., Riedi, J., and Djellali, M. S.: A study of polarimetric error induced by satellite motion: application to the 3MI and similar sensors, *Atmos. Meas. Tech.*, 14, 1801–1816, <https://doi.org/10.5194/amt-14-1801-2021>, 2021.
- Ibrahim, A., Franz, B. A., Sayer, A. M., Knobelspiesse, K., Zhang, M., Bailey, S. W., McKinna, L. I. W., Gao, M., and Werdell, P. J.: Optimal estimation framework for ocean color atmospheric correction and pixel-level uncertainty quantification, *Appl. Opt.*, 61, 6453–6475, <https://doi.org/10.1364/AO.461861>, 2022.
- Jia, H., Quaas, J., Gryspeerdt, E., Böhm, C., and Sourdeval, O.: Addressing the difficulties in quantifying droplet number response to aerosol from satellite observations, *Atmos. Chem. Phys.*, 22, 7353–7372, <https://doi.org/10.5194/acp-22-7353-2022>, 2022.
- Kahn, R.: Satellites and Satellite Remote Sensing | Aerosol Measurements, *Encyclopedia of Atmospheric Sciences*, 2nd edn., edited by: North, G. R., Pyle, J., and Zhang, F., Academic Press, Oxford, 51–66, <https://doi.org/10.1016/B978-0-12-382225-3.00347-9>, 2015.
- Kaufman, Y. J., Tanré, D., and Boucher, O.: A satellite view of aerosols in the climate system, *Nature*, 419, 215–223, <https://doi.org/10.1038/nature01091>, 2002.
- Kawata, Y.: Circular polarization of sunlight reflected by planetary atmospheres, *Icarus*, 33, 217–232, [https://doi.org/10.1016/0019-1035\(78\)90035-0](https://doi.org/10.1016/0019-1035(78)90035-0), 1978.
- Knobelspiesse, K., Cairns, B., Mishchenko, M., Chowdhary, J., Tsigaridis, K., van Diedenhoven, B., Martin, W., Ottaviani, M., and Alexandrov, M.: Analysis of fine-mode aerosol retrieval capabilities by different passive remote sensing instrument designs, *Opt. Express*, 20, 21457–21484, <https://doi.org/10.1364/OE.20.021457>, 2012.
- Koepke, P.: Remote sensing signature of whitecaps, in: *Oceanic Whitecaps and Their Role in Air–Sea Exchange Processes*, edited by: Monahan, E., and Niocaill, G. M., 251–260, Springer, New York, 1986.
- Kokhanovsky, A., Davis, A., Cairns, B., Dubovik, O., Hasekamp, O., Sano, I., Mukai, S., Rozanov, V., Litvinov, P., Lapyonok, T., Kolomiets, I., Oberemok, Y., Savenkov, S., Martin, W., Wasilewski, A., Di Noia, A., Stap, F., Rietjens, J., Xu, F., Natraj, V., Duan, M., Cheng, T., and Munro, R.: Space-based remote sensing of atmospheric aerosols: The multi-angle spectro-polarimetric frontier, *Earth-Sci. Rev.*, 145, 85–116, <https://doi.org/10.1016/j.earscirev.2015.01.012>, 2015.
- Kokhanovsky, A. A.: Parameterization of the Mueller matrix of oceanic waters, *J. Geophys. Res.-Oceans*, 108, 3175, 2003.
- Lacagnina, C., Hasekamp, O. P., and Torres, O.: Direct radiative effect of aerosols based on PARASOL and OMI satellite observations, *J. Geophys. Res.-Atmos.*, 122, 2366–2388, <https://doi.org/10.1002/2016JD025706>, 2017.
- Lang, R., Poli, G., Fougnie, B., Lacan, A., Marbach, T., Riedi, J., Schlüssel, P., Couto, A. B., and Munro, R.: The 3MI Level-1C geoprojected product – definition and processing description, *J. Quant. Spectrosc. Ra.*, 225, 91–109, <https://doi.org/10.1016/j.jqsrt.2018.12.022>, 2019.
- Li, L., Dubovik, O., Derimian, Y., Schuster, G. L., Lapyonok, T., Litvinov, P., Ducos, F., Fuertes, D., Chen, C., Li, Z., Lopatin, A.,

- Torres, B., and Che, H.: Retrieval of aerosol components directly from satellite and ground-based measurements, *Atmos. Chem. Phys.*, 19, 13409–13443, <https://doi.org/10.5194/acp-19-13409-2019>, 2019.
- Li, Z., Hou, W., Hong, J., Zheng, F., Luo, D., Wang, J., Gu, X., and Qiao, Y.: Directional Polarimetric Camera (DPC): Monitoring aerosol spectral optical properties over land from satellite observation, *J. Quant. Spectrosc. Ra.*, 218, 21–37, <https://doi.org/10.1016/j.jqsrt.2018.07.003>, 2018.
- Martins, J. V., Fernandez-Borda, R., McBride, B., Remer, L., and Barbosa, H. M. J.: The HARP hyperangular imaging polarimeter and the need for small satellite payloads with high science payoff for earth science remote sensing, in: *IGARSS 2018 – 2018 IEEE International Geoscience and Remote Sensing Symposium*, Valencia, Spain, 22–27 July, 2018, 6304–6307, <https://doi.org/10.1109/IGARSS.2018.8518823>, 2018.
- McBride, B. A., Martins, J. V., Cieslak, J. D., Fernandez-Borda, R., Puthukkudy, A., Xu, X., Sienkiewicz, N., Cairns, B., and Barbosa, H. M. J.: Pre-launch calibration and validation of the Airborne Hyper-Angular Rainbow Polarimeter (AirHARP) instrument, *EGU sphere* [preprint], <https://doi.org/10.5194/egusphere-2023-865>, 2023.
- Meister, G., Knuble, J. J., Chemerys, L. H., Choi, H., Collins, N. R., Eplee, R. E., Gliese, U., Gorman, E. T., Jepsen, K., Kitchen-McKinley, S., Lee, S., McIntire, J. W., Patt, F. S., Tse, B. C., Waluschka, E., and Werdell, P. J.: Test Results From the Pre-launch Characterization Campaign of the Engineering Test Unit of the Ocean Color Instrument of NASA's Plankton, Aerosol, Cloud and Ocean Ecosystem (PACE) Mission, *Frontiers in Remote Sensing*, 3, 875863, <https://doi.org/10.3389/frsen.2022.875863>, 2022.
- Mishchenko, M. I. and Travis, L. D.: Satellite retrieval of aerosol properties over the ocean using polarization as well as intensity of reflected sunlight, *J. Geophys. Res.-Atmos.*, 102, 16989–17013, <https://doi.org/10.1029/96JD02425>, 1997.
- Mishchenko, M. I., Travis, L. D., and Lacis, A. A.: *Scattering, Absorption, and Emission of Light by Small Particles*, Cambridge University Press, Cambridge, England, ISBN 052178252X, 2002.
- Mishchenko, M. I., Cairns, B., Hansen, J. E., Travis, L. D., Burg, R., Kaufman, Y. J., Vanderlei Martins, J., and Shettle, E. P.: Monitoring of aerosol forcing of climate from space: analysis of measurement requirements, *J. Quant. Spectrosc. Ra.*, 88, 149–161, <https://doi.org/10.1016/j.jqsrt.2004.03.030>, 2004.
- Mukherjee, L., Zhai, P.-W., Gao, M., Hu, Y., A. Franz, B., and Werdell, P. J.: Neural Network Reflectance Prediction Model for Both Open Ocean and Coastal Waters, *Remote Sens.-Basel*, 12, 1421, <https://doi.org/10.3390/rs12091421>, 2020.
- Nanda, S., de Graaf, M., Veefkind, J. P., ter Linden, M., Sneep, M., de Haan, J., and Levelt, P. F.: A neural network radiative transfer model approach applied to the Tropospheric Monitoring Instrument aerosol height algorithm, *Atmos. Meas. Tech.*, 12, 6619–6634, <https://doi.org/10.5194/amt-12-6619-2019>, 2019.
- OB.DAAC: PACE L1C spatial grids, Earth Data [data set], <https://oceansci.gsfc.nasa.gov/directdataaccess/Level-1C/SPACE-spacecraft/2022/080/> (last access: 30 November 2023), 2023a.
- OB.DAAC: PACE L1C ancillary data, Earth Data [data set], <https://oceansci.gsfc.nasa.gov/directdataaccess/Ancillary/SPACE-spacecraft/2022/080/> (last access: 30 November 2023), 2023b.
- OB.DAAC: PACE HARP2 L1C simulated data, Earth Data [data set], <https://oceansci.gsfc.nasa.gov/directdataaccess/Level-1C/PACE-HARP2/2022/080/> (last access: 30 November 2023), 2023c.
- OB.DAAC: PACE HARP2 L2 FastMAPOL product, Earth Data [data set], <https://oceansci.gsfc.nasa.gov/directdataaccess/Level-2/PACE-HARP2/2022/080/> (last access: 30 November 2023), 2023d.
- Osawa, K., Tsuji, Y., Ueno, Y., Naruse, A., Yokota, R., and Matsuoka, S.: Large-Scale Distributed Second-Order Optimization Using Kronecker-Factored Approximate Curvature for Deep Convolutional Neural Networks, *Proceedings of the IEEE/CVF Conference on Computer Vision and Pattern Recognition (CVPR)*, Date of Conference: 15–20 June 2019, <https://doi.org/10.1109/CVPR.2019.01264>, Conference Location: Long Beach, CA, USA, 2019.
- Knobelspiesse, K. D., Patt, F. S., Montes, M. A., Bailey, S. W., Cairns, B., Franz, B. A., Gao, M., and Sayer, A. M.: The PACE Level 1C data format, *PACE Technical Memorandum Series*, NASA/TM – 2023-219027, Vol. 12, in press, 2023.
- Pörtner, H.-O., Roberts, D., Tignor, M., Poloczanska, E., Mintenbeck, K., Alegría, A., Craig, M., Langsdorf, S., Löschke, S., Möller, V., Okem, A., and Rama, B. (Eds.): *IPCC, 2022: Climate Change 2022: Impacts, Adaptation, and Vulnerability. Contribution of Working Group II to the Sixth Assessment Report of the Intergovernmental Panel on Climate Change*, Cambridge University Press, in press, 2023.
- Puthukkudy, A., Martins, J. V., Remer, L. A., Xu, X., Dubovik, O., Litvinov, P., McBride, B., Burton, S., and Barbosa, H. M. J.: Retrieval of aerosol properties from Airborne Hyper-Angular Rainbow Polarimeter (AirHARP) observations during ACEPOL 2017, *Atmos. Meas. Tech.*, 13, 5207–5236, <https://doi.org/10.5194/amt-13-5207-2020>, 2020.
- Randles, C. A., da Silva, A. M., Buchard, V., Colarco, P. R., Darmenov, A., Govindaraju, R., Smirnov, A., Holben, B., Ferrare, R., Hair, J., Shinozuka, Y., and Flynn, C. J.: *The MERRA-2 Aerosol Reanalysis, 1980 Onward. Part I: System Description and Data Assimilation Evaluation*, *J. Climate*, 30, 6823–6850, <https://doi.org/10.1175/JCLI-D-16-0609.1>, 2017.
- Remer, L. A., Davis, A. B., Mattoo, S., Levy, R. C., Kalashnikova, O. V., Coddington, O., Chowdhary, J., Knobelspiesse, K., Xu, X., Ahmad, Z., Boss, E., Cairns, B., Dierssen, H. M., Diner, D. J., Franz, B., Frouin, R., Gao, B.-C., Ibrahim, A., Martins, J. V., Omar, A. H., Torres, O., Xu, F., and Zhai, P.-W.: Retrieving Aerosol Characteristics From the PACE Mission, Part 1: Ocean Color Instrument, *Front. Earth Sci.*, 7, 152, <https://doi.org/10.3389/feart.2019.00152>, 2019a.
- Remer, L. A., Knobelspiesse, K., Zhai, P.-W., Xu, F., Kalashnikova, O. V., Chowdhary, J., Hasekamp, O., Dubovik, O., Wu, L., Ahmad, Z., Boss, E., Cairns, B., Coddington, O., Davis, A. B., Dierssen, H. M., Diner, D. J., Franz, B., Frouin, R., Gao, B.-C., Ibrahim, A., Levy, R. C., Martins, J. V., Omar, A. H., and Torres, O.: Retrieving Aerosol Characteristics From the PACE Mission, Part 2: Multi-Angle and Polarimetry, *Frontiers in Environmental Science*, 7, 94, <https://doi.org/10.3389/fenvs.2019.00094>, 2019b.

- Rodgers, C.: Inverse Methods for Atmospheric Sounding: Theory and Practice, World Scientific World Scientific Publishing, Singapore, <https://doi.org/10.1142/3171>, 2000.
- Schroeder, T., Behnert, I., Schaale, M., Fischer, J., and Doerffer, R.: Atmospheric correction algorithm for MERIS above case-2 waters, *Int. J. Remote Sens.*, 28, 1469–1486, <https://doi.org/10.1080/01431160600962574>, 2007.
- Seegers, B. N., Stumpf, R. P., Schaeffer, B. A., Loftin, K. A., and Werdell, P. J.: Performance metrics for the assessment of satellite data products: an ocean color case study, *Opt. Express*, 26, 7404–7422, <https://doi.org/10.1364/OE.26.007404>, 2018.
- Shi, C., Hashimoto, M., Shiomi, K., and Nakajima, T.: Development of an Algorithm to Retrieve Aerosol Optical Properties Over Water Using an Artificial Neural Network Radiative Transfer Scheme: First Result From GOSAT-2/CAI-2, *IEEE T. Geosci. Remote*, 59, 1–12, <https://doi.org/10.1109/TGRS.2020.3038892>, 2020.
- Shorten, C. and Khoshgoftaar, T. M.: A survey on Image Data Augmentation for Deep Learning, *Journal of Big Data*, 6, 60, <https://doi.org/10.1186/s40537-019-0197-0>, 2019.
- Silverman, B.: Density Estimation for Statistics and Data Analysis, vol. 26, Monographs on Statistics and Applied Probability, Chapman and Hall, London, ISBN 0-412-24620-1, 1986.
- Smit, J. M., Rietjens, J. H. H., van Harten, G., Noia, A. D., Laauwen, W., Rheingans, B. E., Diner, D. J., Cairns, B., Wasilewski, A., Knobelspiesse, K. D., Ferrare, R., and Hasekamp, O. P.: SPEx airborne spectropolarimeter calibration and performance, *Appl. Opt.*, 58, 5695–5719, <https://doi.org/10.1364/AO.58.005695>, 2019.
- Snyder, J. P.: Map projections – A working manual, vol. 1395, US Government Printing Office, <https://doi.org/10.3133/pp1395>, 1987.
- Stamnes, S., Hostetler, C., Ferrare, R., Burton, S., Liu, X., Hair, J., Hu, Y., Wasilewski, A., Martin, W., van Diedenhoven, B., Chowdhary, J., Cetinić, I., Berg, L. K., Stamnes, K., and Cairns, B.: Simultaneous polarimeter retrievals of microphysical aerosol and ocean color parameters from the “MAPP” algorithm with comparison to high-spectral-resolution lidar aerosol and ocean products, *Appl. Opt.*, 57, 2394–2413, <https://doi.org/10.1364/AO.57.002394>, 2018.
- Stamnes, S., Jones, M., Allen, J. G., Chemyakin, E., Bell, A., Chowdhary, J., Liu, X., Burton, S. P., Van Diedenhoven, B., Hasekamp, O., Hair, J., Hu, Y., Hostetler, C., Ferrare, R., Stamnes, K., and Cairns, B.: The PACE-MAPP algorithm: Simultaneous aerosol and ocean polarimeter products using coupled atmosphere-ocean vector radiative transfer, *Frontiers in Remote Sensing*, 4, 1–16, <https://doi.org/10.3389/frsen.2023.1174672>, 2023.
- Stegmann, P. G., Johnson, B., Moradi, I., Karpowicz, B., and McCarty, W.: A deep learning approach to fast radiative transfer, *J. Quant. Spectrosc. Ra.*, 280, 108088, <https://doi.org/10.1016/j.jqsrt.2022.108088>, 2022.
- Tanré, D., Bréon, F. M., Deuzé, J. L., Dubovik, O., Ducos, F., François, P., Goloub, P., Herman, M., Lifermann, A., and Waquet, F.: Remote sensing of aerosols by using polarized, directional and spectral measurements within the A-Train: the PARASOL mission, *Atmos. Meas. Tech.*, 4, 1383–1395, <https://doi.org/10.5194/amt-4-1383-2011>, 2011.
- Ukkonen, P.: Exploring Pathways to More Accurate Machine Learning Emulation of Atmospheric Radiative Transfer, *J. Adv. Model. Earth Sy.*, 14, e2021MS002875, <https://doi.org/10.1029/2021MS002875>, 2022.
- Voss, K. J. and Fry, E. S.: Measurement of the Mueller matrix for ocean water, *Appl. Opt.*, 23, 4427–4439, 1984.
- Wang, J. and Christopher, S. A.: Intercomparison between satellite-derived aerosol optical thickness and PM<sub>2.5</sub> mass: Implications for air quality studies, *Geophys. Res. Lett.*, 30, 2095, <https://doi.org/10.1029/2003GL018174>, 2003.
- Wang, J., Xu, X., Ding, S., Zeng, J., Spurr, R., Liu, X., Chance, K., and Mishchenko, M.: A numerical testbed for remote sensing of aerosols, and its demonstration for evaluating retrieval synergy from a geostationary satellite constellation of GEO-CAPE and GOES-R, *J. Quant. Spectrosc. Ra.*, 146, 510–528, <https://doi.org/10.1016/j.jqsrt.2014.03.020>, 2014.
- Waquet, F., Riedi, J., Labonnote, L. C., Goloub, P., Cairns, B., Deuzé, J.-L., and Tanré, D.: Aerosol Remote Sensing over Clouds Using A-Train Observations, *J. Atmos. Sci.*, 66, 2468–2480, <https://doi.org/10.1175/2009jas3026.1>, 2009.
- Wu, L., Hasekamp, O., van Diedenhoven, B., and Cairns, B.: Aerosol retrieval from multiangle, multispectral photopolarimetric measurements: importance of spectral range and angular resolution, *Atmos. Meas. Tech.*, 8, 2625–2638, <https://doi.org/10.5194/amt-8-2625-2015>, 2015.
- Wu, L., Hasekamp, O., van Diedenhoven, B., Cairns, B., Yorks, J. E., and Chowdhary, J.: Passive remote sensing of aerosol layer height using near-UV multiangle polarization measurements, *Geophys. Res. Lett.*, 43, 8783–8790, <https://doi.org/10.1002/2016GL069848>, 2016.
- Xu, F., Dubovik, O., Zhai, P.-W., Diner, D. J., Kalashnikova, O. V., Seidel, F. C., Litvinov, P., Bovchaliuk, A., Garay, M. J., van Harten, G., and Davis, A. B.: Joint retrieval of aerosol and water-leaving radiance from multispectral, multiangular and polarimetric measurements over ocean, *Atmos. Meas. Tech.*, 9, 2877–2907, <https://doi.org/10.5194/amt-9-2877-2016>, 2016.
- Xu, F., van Harten, G., Diner, D. J., Kalashnikova, O. V., Seidel, F. C., Bruegge, C. J., and Dubovik, O.: Coupled retrieval of aerosol properties and land surface reflection using the Airborne Multiangle Spectropolarimetric Imager, *J. Geophys. Res.-Atmos.*, 122, 7004–7026, <https://doi.org/10.1002/2017JD026776>, 2017.
- Xu, F., Gao, L., Redemann, J., Flynn, C. J., Espinosa, W. R., da Silva, A. M., Stamnes, S., Burton, S. P., Liu, X., Ferrare, R., Cairns, B., and Dubovik, O.: A Combined Lidar-Polarimeter Inversion Approach for Aerosol Remote Sensing Over Ocean, *Frontiers in Remote Sensing*, 2, 620871, <https://doi.org/10.3389/frsen.2021.620871>, 2021.
- Zhai, P.-W. and Hu, Y.: An improved pseudo spherical shell algorithm for vector radiative transfer, *J. Quant. Spectrosc. Ra.*, 282, 108132, <https://doi.org/10.1016/j.jqsrt.2022.108132>, 2022.
- Zhai, P.-W., Gao, M., Franz, B. A., Werdell, P. J., Ibrahim, A., Hu, Y., and Chowdhary, J.: A Radiative Transfer Simulator for PACE: Theory and Applications, *Frontiers in Remote Sensing*, 3, 840188, <https://doi.org/10.3389/frsen.2022.840188>, 2022.